Engineering Structures 291 (2023) 116468

Contents lists available at ScienceDirect

Engineering Structures

journal homepage: www.elsevier.com/locate/engstruct

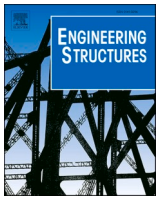

Numerical study on the nonlinear thermomechanical behaviour of refractory masonry with dry joints

Pratik N. Gajjar [a,1], Mahmoud Ali [b,1], Thomas Sayet [b], Alain Gasser [b], Eric Blond [b], João M. Pereira [a,*], Paulo B. Lourenço [a]

[a] University of Minho, ISISE, ARISE, Department of Civil Engineering, Guimarães, Portugal
[b] LaMé Laboratory (EA 7494), Univ. Orléans, Univ. Tours, INSA CVL, 8, rue L. de Vinci, 45072 Orléans, France

ARTICLE INFO

Keywords:
Refractories
Masonry
Numerical modelling
Macro and Micro models
Nonlinear homogenization
Nonlinear analysis
Viscoplasticity

ABSTRACT

Refractory masonry with dry joints is widely employed as a protective lining in industrial applications requiring high-temperature treatments. The thermal and mechanical behaviour of alumina spinel refractory masonry is investigated for a wide range of mechanical loading conditions at ambient and high temperature up to 1500 °C within the framework of the ATHOR project. This paper discusses the different numerical analysis approaches for the simulation of the experimental results. Micro and macro modelling approaches show good agreement with the large scale uniaxial and biaxial compression tests for loading and unloading at the ambient temperature. Simulations carried out for large scale uniaxial and biaxial creep tests as well as biaxial relaxation tests at 1500 °C show good agreement. The numerical results indicate the ability of these modelling approaches to represent the complex thermomechanical behaviour of the refractory masonry. Both methods demonstrate an orthotropic and highly nonlinear behaviour of the refractory masonry as observed in the experimental campaign. The numerical outcome, validated with experimental results demonstrate compatibility between micro and macro modelling approach that can be employed to evaluate local and global behaviour of large industrial installations.

1. Introduction

Refractory masonry structures are extensively employed in various industrial applications operating at high temperatures, such as steel ladles, rotary kilns and furnaces. These refractory materials provide stability with good thermal, chemical and mechanical performance at high temperatures [1]. Refractory masonry in steel ladle linings experiences high cyclic thermal loads, thermal shock, and severe chemical environments [2,3]. Therefore, these linings undergo high thermomechanical loads arising from thermal and mechanical boundary conditions. Such harsh environment leads to in-service degradation and failure of refractory linings [4]. Therefore, increasing the knowledge to allow better predicting the thermomechanical behaviour of such installations is of crucial importance. This is a complex and challenging work in the current engineering praxis due to the interaction between different refractory materials and nonlinear thermomechanical behaviour at high temperatures [5,6].

Refractory materials exhibit complex behaviour. At lower temperatures, their behaviour is quasi-brittle, while at high temperatures, it becomes ductile [4]. Due to this behaviour and the challenging environment in which these materials usually work, understanding failure mechanisms and thermal damages of the refractories becomes essential [7,8]. The importance of the occurrence of creep for refractories in industrial applications has been shown in previous research [9,10]. The same can be described for the corrosion of refractories; its existence is known and studied extensively [11,12].

Typically in a steel ladle, mortarless masonry (also known as dry-stacked masonry) is used for the linings [13]. The arrangement of refractory bricks and the dimension tolerances of the bricks leave small gaps between the bricks' faces, defined as a dry joint. The behaviour of this joint depends on surface roughness and geometric imperfections [14–16]. Material discontinuity induced by the dry joints and its cyclic opening and closing behaviour alters the macroscopic behaviour of the masonry [17–19]. The global structure exhibits an orthotropic and

* Corresponding author.
E-mail address: jpereira@civil.uminho.pt (J.M. Pereira).
[1] P.N.G and M.A. contributed equally to this work.

https://doi.org/10.1016/j.engstruct.2023.116468
Received 3 January 2023; Received in revised form 23 May 2023; Accepted 9 June 2023

nonlinear response different from the behaviour of base refractory materials [20]. Therefore, extensive investigations are required to optimise the design of such linings. Large-scale experimental campaigns are limited in this field due to high cost, technical complexities and severe working conditions involved. Thus, numerical models must be employed to study the global behaviour of mortarless refractory masonry, which can be validated with the available experimental outcomes [21–23].

Several modelling strategies were developed in the literature to simulate mortarless masonry structures. Limit analysis and discrete element modelling (DEM) can be employed to evaluate the collapse mechanism of masonry walls subjected to various mechanical loading [24–28]. Finite element modelling and DEM are widely used for the structural analysis of heritage structures usually built with masonry [29–31]. Furthermore, surrogate models can also be used in combination with these approaches to characterise behaviour of complex numerical simulation to significantly reduce computational cost [32]. However, these approaches are mainly focused on structures at ambient temperatures. Finite element modelling (FEM) is widely used for masonry structures operating at various temperatures. FEM can be employed from a micro-scale to a super large scale [33]. In the so-called micro-models (even if meso-models would be a better choice of wording), bricks and joints (mortar or mortarless) are modelled separately while in macro-models, bricks and joints are replaced by a homogenised equivalent material. For a realistic representation of the behaviour of a structure, a comprehensive set of material parameters is needed. Given the complexity involved, most studies encompass more straightforward techniques in numerical simulation of refractory masonries, such as linear thermo-elasticity. Limited work is available where more complex models, including viscoplasticity and damage, are utilised [22,34–36]. These models are usually used to simulate small-scale experiments, mainly due to expensive computational costs and solution convergence problems. However, micro-models provide valuable information regarding localised behaviour (stress/strain concentration, localised damage, etc.) when detailed material parameters are used.

Macro-models utilising homogenised material approaches can be used to overcome the challenges of micro-modelling. However, for mortarless refractory masonry, few studies exist that address this modelling approach. Nguyen et al. [18] developed and validated a homogeneous equivalent material model by replacing the bricks and joints with an equivalent material to simulate mortarless refractory masonry structures. The bricks are considered to obey isotropic linear elasticity. The model considers the influence of joint closure on the homogeneous mechanical response of the system. Ali et al. [20,37] further developed the multiscale numerical model with viscoplasticity that promotes a better understanding of the nonlinear mechanical behaviour of refractory masonry structures at high temperatures. This macro-model can be used to simulate large structures with reasonable computational costs.

This study aims to perform numerical analyses to validate micro and macro-modelling approaches with the experimental results gathered by Ali et al. [38]. These tests were performed with different loading conditions at ambient and high temperatures (1500 °C). The numerical models in this study employ the elastic-viscoplastic behaviour of the refractory material to simulate the response of the mortarless masonry wall. The framework of these modelling approaches is available in literature discussed earlier. Micro modelling offers detailed and accurate representations but demands significant computational efforts and detailed input data. While macro modelling provides computational efficiency and simplicity but sacrifices detailed information and may not capture localised effects accurately. Additionally, performance of these approaches has not been validated with large-scale experimental data for a mortarless refractory masonry.

Therefore, this study presents a comprehensive analysis to compare the outcome of both modelling approaches in detail to check the accuracy of results. The results obtained from these models validate the key parameters necessary for analysis of such masonry, dry joint behaviour and viscoplastic behaviour of the material at high temperature, which is not present in current literature. This validation will assist in developing coherent modelling approaches needed to design large industrial structures with mortarless refractory masonry.

The present paper is organised as follows. In section 2, a description of the mortarless refractory masonry structure and critical thermo-mechanical properties is presented. In section 3, a detailed description of the micro and macro modelling approaches is discussed, along with joint closure and reopening criteria. Verification of the numerical models and results of mortarless refractory masonry walls subjected to ambient and high temperatures are presented and discussed in sections 4 and 5, respectively. Key findings of the present study and conclusions are given in Section 6.

2. Mechanical and physical properties

In the experimental campaign carried out by Ali et al. [38], mortarless masonry built up with alumina spinel bricks (150 × 100 × 140 mm^3) was subjected to various loading conditions at ambient and high temperatures. A schematic overview of the test setup used is presented in Fig. 1. The test setup consists of a monolithic reaction frame in which the hydraulic jacks, loading beams, LVDTs and heating system were connected. Additional details regarding the experimental setup, the tested specimens and the acquisition system can be found in [38]. Thirteen tests were performed on alumina spinel walls. Six tests were performed at room temperature and the remaining seven tests were carried out at high temperature. The test series names, loading conditions in directions perpendicular to the surfaces of bed and head joints and testing temperature are given in Table 1. For all tests, the dimensions of the walls are 1125 × 1100 × 140 mm^3.

Alumina spinel material has temperature dependent thermal and mechanical properties. The Young's modulus [39], and the ultimate compressive stress [16] variations with temperature are presented in Fig. 2a and b, respectively. The coefficient of thermal expansion of the material is 8.87 × 10^{-6} K^{-1} [40]. The friction coefficient between alumina spinel bricks has been characterized by Oliveira et al. [16] at different temperatures and reported in Table 2. Detailed thermal and mechanical properties of this material can be found in [16,38,40,41].

The creep behaviour of the material was characterized within the framework of the ATHOR project. The creep parameters were identified by Samadi et al. [6] and Teixeira et al. [10] at three different temperatures, namely: 1300 °C, 1400 °C and 1500 °C. They are reported in Table 3 (A, n and m are the constants of the Norton-Bailey creep law [42]). The Norton-Bailey creep law is shown in Equation (1). The equivalent creep strain rate ($\dot{\varepsilon}_{cr}$), which is a scalar, is a function of the equivalent von Mises stress (q) and the total equivalent creep strain (ε_{cr}).

$$\dot{\varepsilon}_{cr} = (Aq^n[(m+1)\varepsilon_{cr}]^m)^{\frac{1}{m+1}} \quad (1)$$

To verify whether creep is significant for temperatures below 1300 °C, four compressive creep tests (at 1200 °C and 1000 °C, each temperature repeated twice) were carried out [39]. The results of these tests are compared with the results of compressive creep tests at higher temperatures [6,10] in Fig. 3. It can be noticed that for temperatures below 1200 °C and for the studied compressive stress level (6 MPa, maximum load used in the large-scale creep and relaxation tests reported later in this work), the creep of the material is insignificant. All the material properties mentioned above were used for building both the micro and macro-modelling approaches.

3. Modelling approaches

Masonry structures are composed of units and joints. They feature a wide variety of combinations with different component materials, geometry, and textures. These combinations imply a significant number of descriptive material parameters, thus, being a complex research field

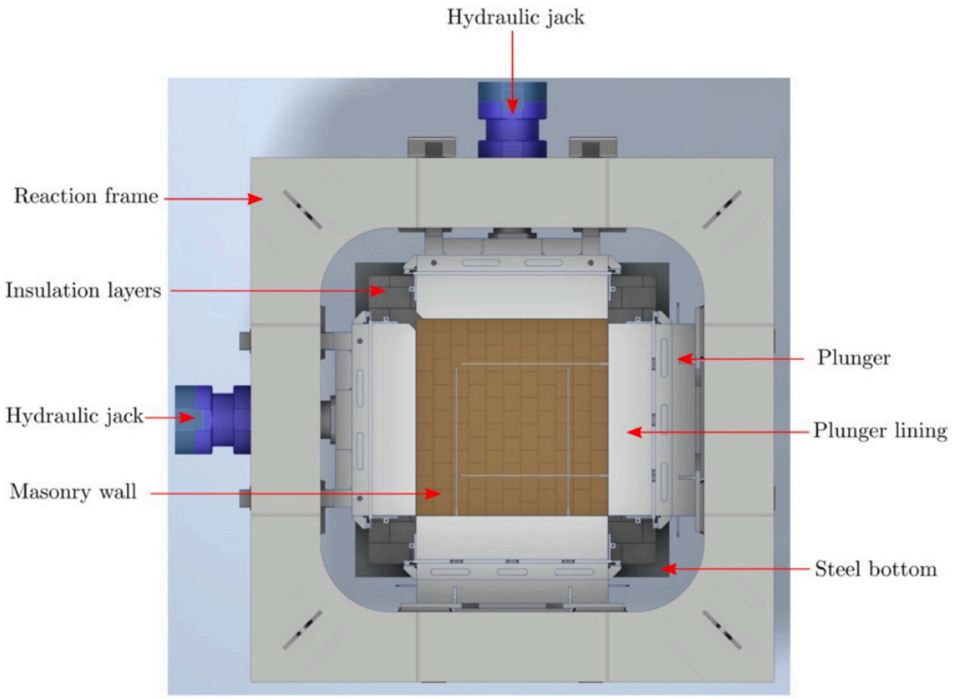

Fig. 1. Top view of the biaxial compression test field [38].

Table 1
Summary of the biaxial compression tests of refractory masonry walls performed at room and high temperatures [38].

Series	Specimen	Maximum load		Temperature
		Bed	Head	
S01	S01 - 01	6 MPa	Constrained	Room temperature
	S01 - 02			
S02	S02 - 01	Constrained	6 MPa	
	S02 - 02			
S03	S03 - 01	6 MPa	6 MPa	
	S03 - 02			
S04	S04 - 01	4 MPa	Constrained	High temperature
	S04 - 02			
S05	S05 - 01	Constrained	4 MPa	
S06	S06 - 01	4 MPa	4 MPa	
	S06 - 02			
S07	S07 - 01	4–6 MPa	4–6 MPa	
	S07 - 02			

[43]. Therefore, the importance of sophisticated numerical tools capable of predicting the behaviour of the masonry from the linear stage, through cracking and degradation until complete loss of strength is paramount [44]. In the 1990s, the masonry research community began to show interest in sophisticated numerical tools to study masonry instead of the prevailing tradition of rules-of-thumb and empirical formulae [45].

As a composite material, masonry has certain particularities that make it challenging to adapt existing numerical tools from more advanced research fields, such as the mechanics of concrete, rock, and other materials [45]. The numerical approach for masonry can focus on the micro-modelling of the individual components or the macro-modelling of masonry as a composite. Depending on the level of accuracy and the simplicity desired, it is possible to use the different modelling strategies, see Fig. 4 [44].

In the first approach, mechanical properties of both the unit and mortar and the interface between them must be considered (Fig. 4a). Alternatively, a simplified micro-modelling approach (Fig. 4b) can be adopted. In the simplified procedure, the units are expanded by adding the mortar thickness. The expanded units are modelled as a series of continuum elements. The interaction between the expanded units is modelled as a series of interface elements. However, some accuracy is lost since Poisson's effect of the mortar is not included [44]. These micro-modelling approaches are certainly capable of well reproducing orthotropic behaviour of masonry but are characterised by long processing times, being only recommended for limited size structural problems [33,46–48].

In the case of large structures (such as steel ladles), the knowledge of the interaction between units and mortar can be negligible for global structural behaviour. Therefore, a different approach, denoted macro-modelling, can be used. In this approach, the material is regarded as an anisotropic composite, and a relation is established between average masonry strains and average masonry stresses (Fig. 4c). This is a phenomenological approach, meaning that the material parameters must be derived in masonry tests of sufficiently large size under homogeneous states of stress. A complete macro-model must reproduce an orthotropic material with different tensile and compressive strengths along the material axes and different inelastic behaviour for each material axis [45].

One modelling strategy cannot be preferred over the other because different application fields exist for micro and macro-models. Micro-modelling is necessary to give a better understanding about the local behaviour. In contrast, macro-modelling is more practice oriented due to the reduced time and memory requirements as well as a user-friendly mesh generation [44].

3.1. Micro-modelling approach

One of the modelling approaches used to simulate the experimental results was a simplified micro-modelling approach (Fig. 4b), and is described next. In this approach, the spatial discretization of the masonry is performed at the level of brick elements, and the dry joints are represented by their contact behaviour using interface elements. Herein, brick elements are simulated with corresponding mechanical parameters of the material from which they are made and their connection is simulated with contact elements that allow separation, penetration, and sliding at the contact.

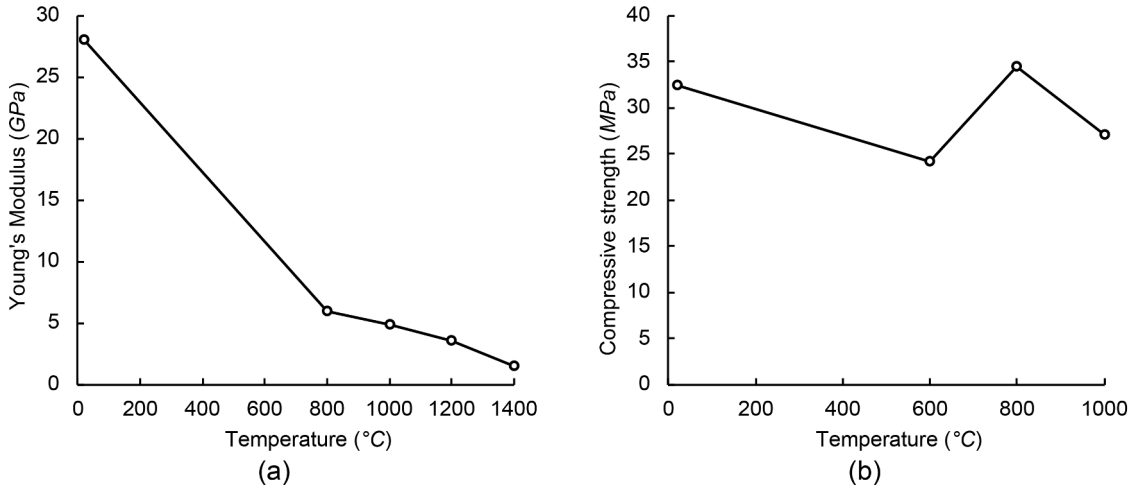

Fig. 2. Mechanical properties of alumina spinel bricks tested in the present work: a) Young's modulus [39]; b) ultimate compressive strength [16].

Table 2
Friction coefficient values for dry joints at different temperatures [22].

Temperature (°C)	20	300	600	900
Friction coefficient (-)	0.60	0.50	0.51	0.53

Table 3
Creep parameters of alumina spinel refractory materials at different temperatures [6,10].

Temperature (°C)	Primary creep			Secondary creep	
	A (MPa $^{-n}$ s^{-1})	n	m	A (MPa $^{-n}$ s^{-1})	n
1300	3.89×10^{-15}	4.25	−2.73	1.25×10^{-12}	6.45
1400	1.25×10^{-14}	5.80	−2.65	1.62×10^{-12}	9.20
1500	1.62×10^{-10}	2.00	−1.97	1.32×10^{-9}	5.84

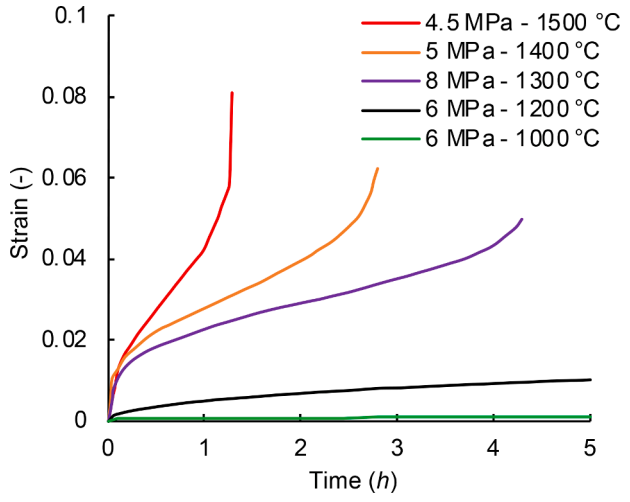

Fig. 3. Creep behaviour of alumina spinel refractory material at different temperatures and compressive stress levels [6,10,39].

Considering the mortarless refractory masonry, under the scope of this work, the units are modelled as continuum elements in the micro-modelling approach. The joints between bricks are represented by interface elements. Even though accurate results are obtained using the micro-modelling technique, the main drawback is the extensive computational resources required to run the analysis [19,49]. Nevertheless, this approach provides detailed results on the behaviour of the bricks and joints. Therefore, it was adopted in this study. The numerical analyses for this approach are performed using the finite element software Abaqus [42]. This is an extensive multi-purpose finite element software package that can be utilised in a wide range of engineering sectors.

For the brick elements, several existing material models might be considered. The simplest one is linear elasticity, which is not able to represent certain particularities of the refractory behaviour but is capable of reproducing expected results within delimitated applications. Another possibility is the concrete damage plasticity (CDP) model, which assumes that failure under compressive crushing and tensile cracking is defined by damage plasticity, using the concept of isotropic damage evolution for representing the inelastic behaviour of concrete-like materials. The CDP model is a modification of the Drucker-Prager model [50,51]. However, the failure surface's shape does not need to be a circle in the deviatory plane. Different damage models for materials are available in literature apart from CDP, such as, Total strain crack model [52] and Mazars [53], along with different optimisation methods based on Levenberg – Marquardt Algorithm, Genetic Algorithm and algorithm of Broyden – Fletcher – Goldfarb – Shanno [54]. Creep plays an essential role in refractory materials' behaviour at high temperatures and the Power-law model can be used to simulate it.

Currently, the software does not allow using the CDP model with the creep model. There are some material subroutines available that combine the effects of damage elasticity and viscoplasticity [55]. However, only commercially available constitutive models were used in the present study (i.e. linear elasticity at ambient temperature and linear elasticity with viscoplasticity at high temperature). This option was employed due to the lower level of forces applied in the experiments and to be consistent with the macro modelling approach where only elastic-viscoplastic behaviour was used. The temperature-dependant primary creep parameters (Table 3), alongside the thermal and elastic properties (Fig. 2) are used to describe the behaviour of alumina spinel refractory bricks used in the simulation.

The presence of joints significantly impacts the behaviour of dry-stacked masonry. The interface elements used to represent the dry joints permit discontinuities in the displacement field. Their behaviour is described as a relation between the stresses and relative displacements across the interface [56]. The dry joints between the brick units are modelled as surface-to-surface contacts in Abaqus. For the normal behaviour of the joints, a tabular form of stress-joint closure values is used. According to Ngapeya et al. [49], increasing the height and length of the wall statistically reduces its effective section (where contact occurs). Therefore, different relations should be used to represent masonry

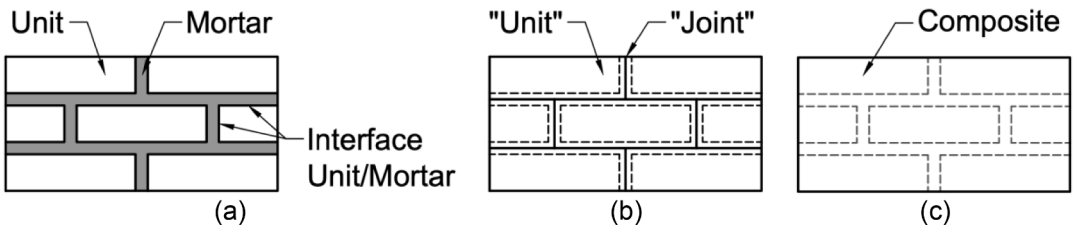

Fig. 4. Modelling strategies for masonry structures (adapted from [44]): a) detailed micro-modelling; b) simplified micro-modelling; c) macro-modelling.

with different dimensions and different producers, as size, geometrical tolerance and material play a role. Different joint overclosure diagrams are shown in Fig. 5 [22]. The values derived from the red profile (Wallet 1350 × 140 mm) are used in this study, as its dimensions are closest to the dimensions of the masonry wall used in this study.

The tangential behaviour is represented by the shear stress-shear relative displacement diagram, which is obtained from the application of the Coulomb criterion [57], defined in Equation (2), where τ is the shear strength, c is the shear strength at zero vertical load stress (usually denoted by cohesion), σ is the normal stress and μ is the friction coefficient or tangent of the friction angle. For dry joints, the cohesion is zero. The friction coefficient of the alumina bricks as a function of the temperature was obtained by Oliveira et al. [16], as shown in Table 2. These values are used for the joints between the bricks.

$$\tau = c + \mu\sigma \tag{2}$$

3.2. Macro modelling approach

Refractory masonry with dry joints has strongly nonlinear stress–strain relationships due to gradual closure of joints and markedly orthotropic behaviour (caused by the difference between the number of bed and head joints and the fact that they can be closed in one direction and open in the other direction). To numerically capture such nonlinear phenomena and consider the impact of gradual joint closure/reopening on the homogenized mechanical response, four periodic joint patterns, as well as transition criteria between them, were defined as depicted in Fig. 6. Each pattern is associated with a specific state of bed and head joints (open or closed) and represents different periodic masonry structure with different equivalent elastic viscoplastic behaviour. The predefined patterns are:

- Pattern AC: All joints are Closed.
- Pattern BO: Bed joints are Open.

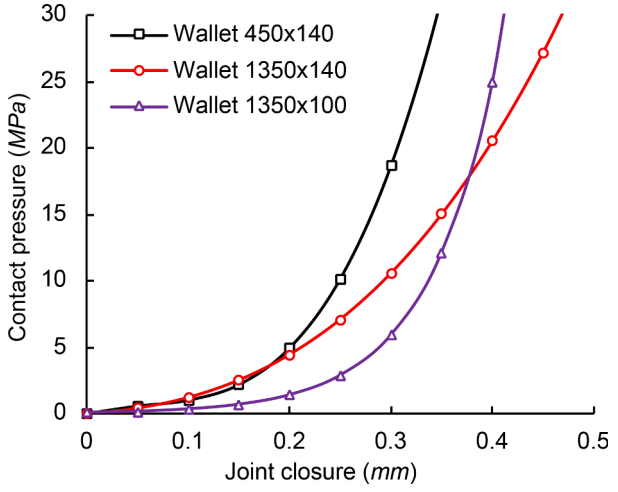

Fig. 5. Contact pressure-overclosure relations used for different wall dimensions (adapted from [22]).

- Pattern HO: Head joints are Open.
- Pattern AO: All joints are Open.

3.2.1. Nonlinear homogenization

The homogenized elastic-viscoplastic behaviour of the four periodic joint patterns were obtained using the FE-base nonlinear homogenization technique [20]. First, a Representative Volume Element (RVE) with volume (V_{UC}) was selected from each periodic joint pattern. Next, periodic boundary conditions were applied to the boundary surfaces of the RVE and three uniaxial and three simple shear loading simulations were performed on it to characterize its homogenized elastic viscoplastic behaviour. The average stresses and strains were calculated by averaging the local stress and strain fields in the RVE. Finally, the homogenized elastic and viscoplastic behaviours were determined, and the macroscopic elastic and viscoplastic tensors were obtained [39].

The homogenized elastic behaviour of the four joint patterns can be described using the orthotropic forms of Hooke's law as [58]:

$$\overline{\overline{\Sigma}} = \overline{\overline{\overline{\overline{C^e}}}} : \overline{\overline{E^e}} \tag{3}$$

where $\overline{\overline{\Sigma}}$, $\overline{\overline{\overline{\overline{C^e}}}}$, and $\overline{\overline{E^e}}$ are the second order macroscopic stress tensor, fourth order effective elastic stiffness tensor and the second order macroscopic elastic strain tensor, respectively. The macroscopic stress tensor can be obtained by averaging the local stress tensor ($\overline{\overline{\sigma}}$) over the volume of the RVE according to:

$$\overline{\overline{\Sigma}} = \langle \overline{\overline{\sigma}} \rangle = \frac{1}{V_{UC}} \int_{V_{UC}} \overline{\overline{\sigma}} dV \tag{4}$$

In the absence of gaps or cracks, the macroscopic elastic strain tensor can be determined as the volume average of the local elastic strain tensor ($\overline{\overline{\varepsilon^e}}$) as:

$$\overline{\overline{E^e}} = \langle \overline{\overline{\varepsilon^e}} \rangle = \frac{1}{V_{UC}} \int_{V_{UC}} \overline{\overline{\varepsilon^e}} dV \tag{5}$$

In the presence of gaps or cracks, the components of the macroscopic elastic strain tensor are calculated from the displacements of the RVE's corners and the initial dimensions of the RVE. Using three uniaxial and three shear loading conditions, and after solving the boundary value problem of each simulation case, the 9 non-zero components of $\overline{\overline{\overline{\overline{C^e}}}}$ were calculated.

To consider the gradual increase in the effective stiffness with the gradual closure of joints and reproduce the strain stiffening behaviour, the joints were reduced to an interface, at the RVE level – micro-modelling (see Fig. 7), with a small thickness (t_i) where the constitutive normal and shear behaviours of the joints have been implemented. The behaviour law of the interface is expressed in incremental form as:

$$\Delta\sigma = k(u)u \tag{6}$$

or,

$$\Delta \begin{Bmatrix} \sigma_n \\ \tau_x \\ \tau_y \end{Bmatrix} = \begin{bmatrix} k_n(u) & 0 & 0 \\ 0 & k_{sx}(u) & 0 \\ 0 & 0 & k_{sy}(u) \end{bmatrix} \Delta \begin{Bmatrix} u_n \\ u_x \\ u_y \end{Bmatrix} \tag{7}$$

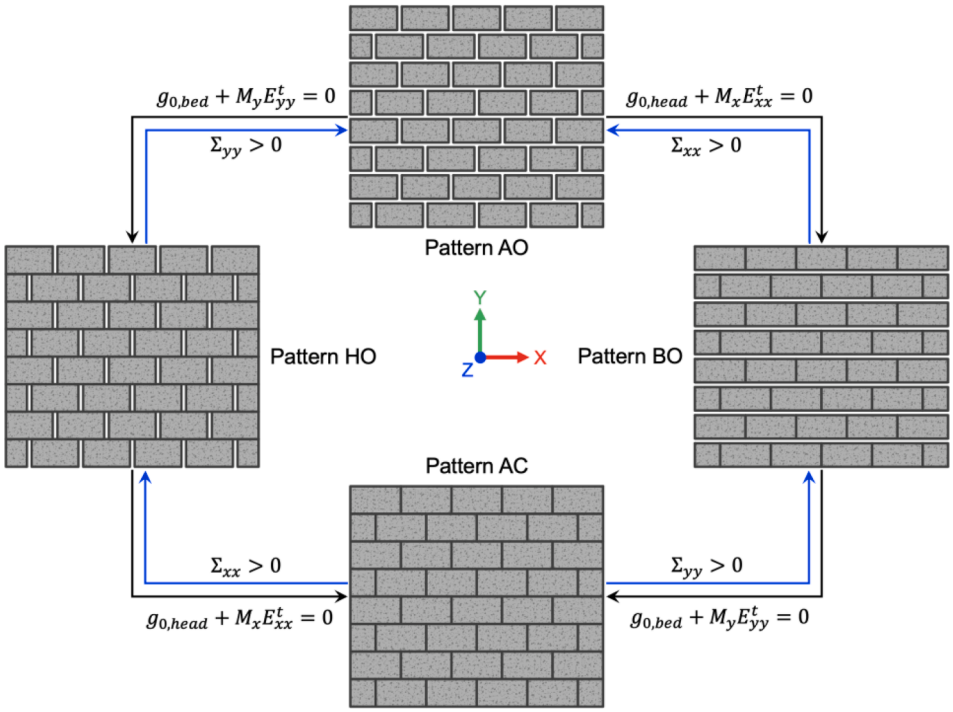

Fig. 6. Schematics of all possible joint patterns of refractory masonry with dry joints and joint closure and opening criteria (adapted from [20]).

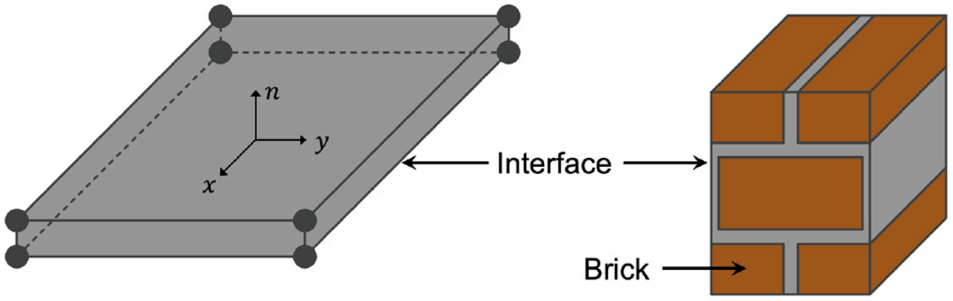

Fig. 7. Schematic of RVE in pattern AO showing the physical model, brick and interface.

where σ_n is the normal stress, and τ_x and τ_y are the transverse stresses in the X and Y directions, respectively (see the coordinate system in Fig. 7). k_n, k_{sx} and k_{sy} are the joint stiffnesses in the normal (n) and shear directions (x, y), respectively. u_n is the normal deformation of the joint or joint closure. u_x and u_y are the shear deformations of the joint.

The variations of k_n with the joints closure (u_n) can be obtained either from classical joints closure tests (two small parts of the bricks are used as a specimen) or uniaxial compression tests of running bond masonry, while k_{sx} and k_{sy} are expressed as [59]:

$$k_{sx}(u) = k_{sy}(u) = \frac{k_n(u_n)}{2(1+\nu)} \tag{8}$$

Classical joint closure tests of two small alumina spinel parts were performed by Oliveira et al. [16] (see Fig. 8a). The main limitation of these tests is that they do not consider the dimension and geometric tolerance of the bricks, and, therefore, in most cases, underestimate joints closure [39]. In the present work and as shown in Fig. 8b, the average closure of joints at different stress levels was studied at three different locations (top, middle and bottom) in a small wall subjected to uniaxial compression load in the direction normal to bed joints up to rupture [22].

The relative displacements between each set of the horizontal lines in the Fig. 8b (top, middle and bottom – note that each set compromises two lines, one above and one below the joints) are obtained from the DIC analysis. For each line in each set, the displacements of 30 points were determined. The joint closure was considered as the relative displacement between the two lines in each set. The joint closure variations with the applied stress at different locations in the wall, as well as the average of the three studied locations are given in Fig. 9a. Comparisons with the results of the classical joints closure test are reported in the same figure.

The stresses are considered as uniform in the wall. Indeed, in reality, they are nonuniform due to the non-flatness of the top course of the wall and stress concentrations caused by the dimension and shape tolerances of the bricks. From Fig. 9a, it can be noticed that at the same stress level, the classical joint closure tests underestimate the joint closure. The calculated average normal and shear stiffnesses of the dry joints are reported in Fig. 9b. They are calculated as following: the average joint closure of the three locations-stress relationship (DIC - Average in Fig. 9a) was fitted. Then, the normal (k_n) and shear ($k_{sx} = k_{sy}$) stiffnesses were calculated using equations (7) and (8) ($\nu = 0.2$).

The compressible and orthotropic (due to the presence of joints) homogenized viscoplastic behaviour of each joint pattern is obtained by averaging the viscoplastic strain ($\overline{\overline{\varepsilon^{vp}}}$) and the local stress ($\overline{\overline{\sigma}}$) tensors over the volume of the RVE and using a localization tensor ($\overline{\overline{\overline{\overline{N}}}}$) according to [60,61]:

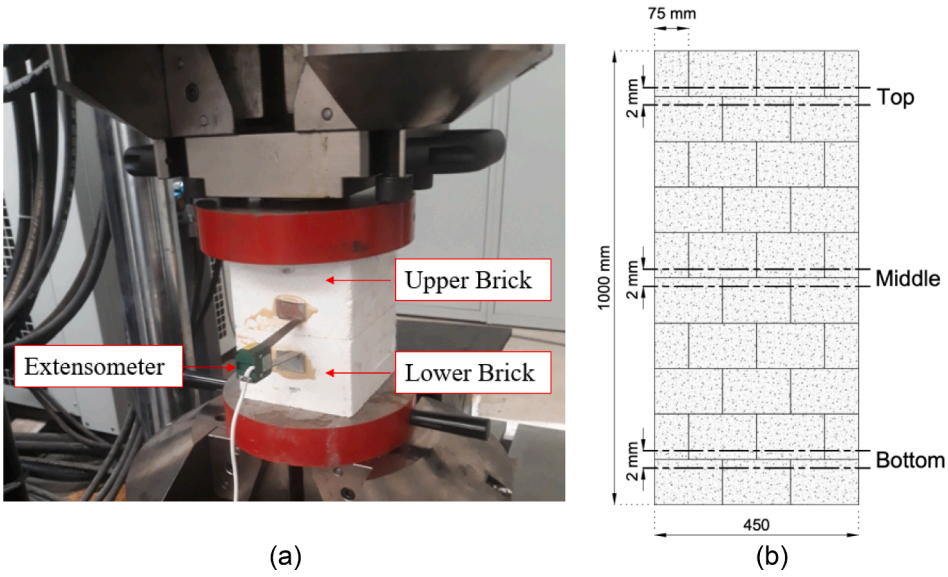

Fig. 8. Joint closure test: a) classical joints closure test on two alumina spinel parts [16]; b) schematic showing small wall subjected to uniaxial compression up to rupture and the chosen areas for studying joints closure by DIC.

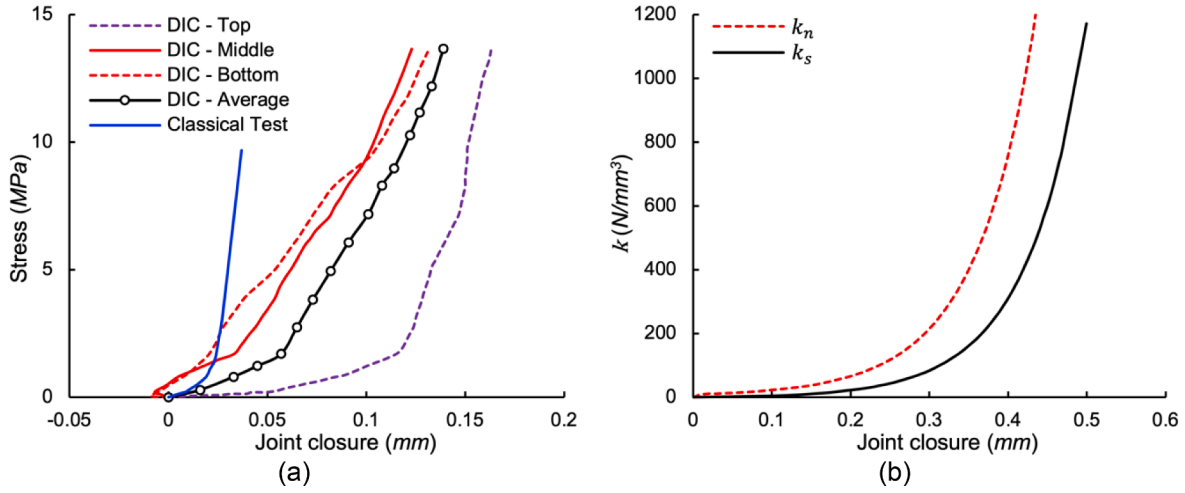

Fig. 9. Joint closure behaviour: a) comparisons between stress variations with joint closure at different locations of the wall and results of classical joints closure test; b) calculated average normal and shear stiffness of the joints.

$$\overline{\overline{\dot{E}^{vp}}} = \frac{1}{2} A \left(\Sigma_{eq}\right)^{n-1} \overline{\overline{\overline{\overline{N}}}} : \overline{\overline{\Sigma}} \tag{9}$$

Here, A and n are the creep parameters of the bricks, Σ_{eq} and $\overline{\overline{\overline{\overline{N}}}}$ are the macroscopic equivalent stress and a fourth order tensor with the same meaning of the localization tensor. The $\overline{\overline{\overline{\overline{N}}}}$ tensor accounts for the orthotropy and compressibility of the structure and enables using the creep parameters of the constitutive material (i.e. bridging between the micro and macro scales). Due to the symmetry of $\overline{\overline{\overline{\overline{N}}}}$ [39], the same can be reduced to a 6 × 6 matrix using the Voigt notations [58] as:

$$\overline{\overline{N}} = \begin{bmatrix} N_{11} & N_{12} & N_{13} & 0 & 0 & 0 \\ N_{12} & N_{22} & N_{23} & 0 & 0 & 0 \\ N_{13} & N_{23} & N_{33} & 0 & 0 & 0 \\ 0 & 0 & 0 & N_{44} & 0 & 0 \\ 0 & 0 & 0 & 0 & N_{55} & 0 \\ 0 & 0 & 0 & 0 & 0 & N_{66} \end{bmatrix} \tag{10}$$

The macroscopic equivalent stress is expressed as [60,62]:

$$\Sigma_{eq} = \sqrt{\frac{1}{2}(\overline{\overline{\Sigma}})^T : \overline{\overline{\overline{\overline{N}}}} : \overline{\overline{\Sigma}}} \tag{11}$$

By combining Equations (9) to (11) and performing six creep simulations at the RVE level (three uniaxial and three shear loading conditions), solving the boundary value problem and calculating the volume average stress and viscoplastic strain tensors, the nine non-zero components of $\overline{\overline{N}}$ can be obtained [20].

3.2.2. Joints closure and reopening

In normal operating conditions, refractory masonry structures undergo cyclic mechanical or thermomechanical loading and unloading. Therefore, the dry joints (bed or head) close and reopen and the structure changes from one pattern to another leading to a change in its homogenized elastic viscoplastic behaviour. This change has been considered by defining joint closure and reopening criteria.

Initially, all joints are open and the structure can be fully described by pattern AO (all open). When subjected to compressive loads or heating, the thickness of the joints decreases gradually from an initial

value (g_0) to zero. As a result, the structure changes from pattern AO to either pattern BO (when head joints close) or pattern HO (when bed joints close). If all joints close, the structure changes from pattern AO to pattern AC (all closed). The joints can be considered as either open or closed based on their instantaneous thickness (g) as:

$$\text{Joint open if } g > 0 \tag{12}$$

The, instantaneous joints thicknesses (g_{bed} and g_{head}) can be expressed in terms of initial joints thicknesses ($g_{0,\text{ bed}}$ and $g_{0,\text{ head}}$) and macroscopic in-plane total strains (E^{t}_{xx} and E^{t}_{yy}) as:

$$\begin{aligned} g_{\text{head}} &= g_{0,\text{ head}} + M_x E^{t}_{xx} \\ g_{\text{bed}} &= g_{0,\text{ bed}} + M_y E^{t}_{yy} \end{aligned} \tag{13}$$

Here, the X and Y directions are the directions of bed joints and head joints, respectively. M_y and M_x are the height and the length of the bricks. The joint closure criteria are given in Fig. 6. Regarding the joint reopening criterion, dry joints can reopen if the normal stress to the surface of the joint is higher than zero (i.e. tensile). The constitutive material model presented in Fig. 6 was implemented into Abaqus through a user material subroutine (UMAT).

4. Numerical analyses at ambient temperature

Using Abaqus finite element software, a series of numerical models of masonry walls subjected to cyclic in-plane uniaxial and biaxial compression loads at room temperature were developed. The purpose of these models was to reproduce the observed experimental behaviour and validate the numerical models. In this section, only the elastic properties (Fig. 2a) of the bricks were used as the tests were performed at ambient temperature, with all nonlinear behaviour concentrated in the joints. The experimental tests were modelled with the two different approaches: the micro modelling and the macro modelling approaches. Both approaches used the same material properties described in Section 2.

The micro and macro FE models of the walls are shown in Fig. 10. The X direction (1125 mm) is the direction normal to head joints, while the Y direction (1100 mm) is normal to bed joints. The four ceramic plates and the insulation layer (ground) of the test setup have been modelled as rigid plates. The units (refractory bricks) and dry joints were modelled separately in the micro-model approach (Fig. 10a). In the macro-model, the wall (bricks and joints) was replaced by a homogeneous material (Fig. 10b) whose mechanical properties depend on the state of the bed and head joints (open or closed). In both models, the walls were meshed with 3D hexahedron elements with 37.5 × 33.33 × 35 mm^3 size. This element size was also selected considering the thermomechanical problem (discussed in section 5), especially in the Z direction due to the thermal gradient and temperature-dependant mechanical properties. Frictional interactions between the contact surfaces of the wall and the fixed rigid plates, moving rigid plates and the ground were considered with a friction coefficient of 0.5.

During the test, the forces were applied though the moving plungers attached with hydraulic jacks (as shown in Fig. 1). These moving plungers are represented by rigid moving plates in numerical models (Fig. 10). Two plungers used as supports during the test are represented by the fixed plungers in the models. The masonry wall was built on the insulating ground which is represented by the rigid ground plate. The connection between the plates and masonry wall is defined by the hard contact (which transfers normal compressive forces and allows separation to satisfy no tensile stresses in interface) to accurately model the experimental conditions. For all the test series, two fixed plates and ground plate are subjected to fixed boundary conditions (no translation and rotation). For the moving plates in X direction, only the translation in that direction is allowed and translation in other two directions is fixed along with rotation in all three directions. Similar boundary conditions are applied for moving plate in Y direction. However, depending on the test series, translation of moving plates is restricted to represent the experimental setup. The configuration of such conditions is described for each test series with a graphical representation in following sections.

4.1. Test series S01 - uniaxial loading and unloading - normal to bed joints

In this test series, two refractory masonry walls were tested [38]. A uniaxial compression load/unload (up to 6 MPa) was applied in the direction normal to bed joints, and the plungers constrained the direction normal to head joints. The boundary conditions for two fixed rigid plates, the rigid moving plate normal to head joints (X direction in Fig. 11a) and the ground are set to fully fixed.

Comparisons between the experimental and numerical force–displacement diagrams of masonry walls subjected to uniaxial compression loading/unloading in the direction normal to bed joints are presented in Fig. 11b. The displacement values were obtained from the relative displacements of the red points shown in Fig. 11a (as in the experiments). It can be seen that the present numerical models reproduce with reasonable accuracy the displacement stiffening mechanical behaviour of the wall. The reaction force increases with the increase in the applied displacement due to the gradual closure of the joints and the increase in effective stiffness and contact area with the closure of joints. After unloading, the wall did not recover its initial configuration. There was permanent deformation caused by the closure of joints, the deformation and the crushing of the asperities present at the contact surfaces of bed joints.

Fig. 12a and b present the numerical displacement fields obtained from the micro and macro-models at the maximum load level (630 kN).

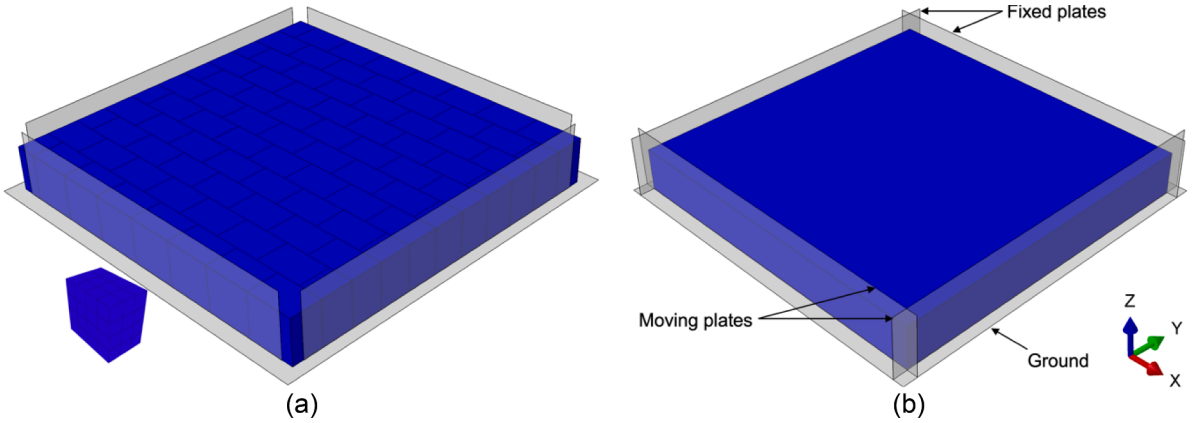

Fig. 10. FE models of the mortarless refractory masonry walls: a) micro-model; b) macro-model.

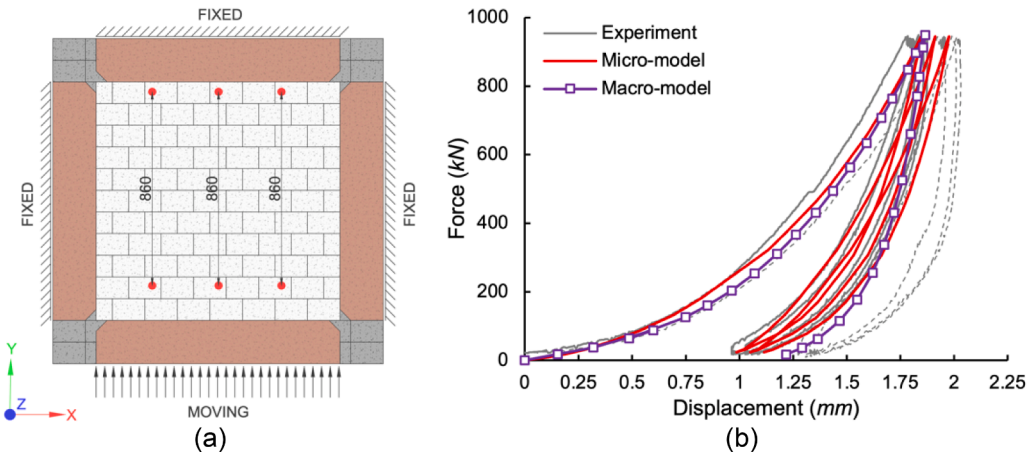

Fig. 11. Test series S01 - uniaxial loading and unloading - normal to bed joints: a) boundary conditions; b) experimental and numerical force–displacement diagrams.

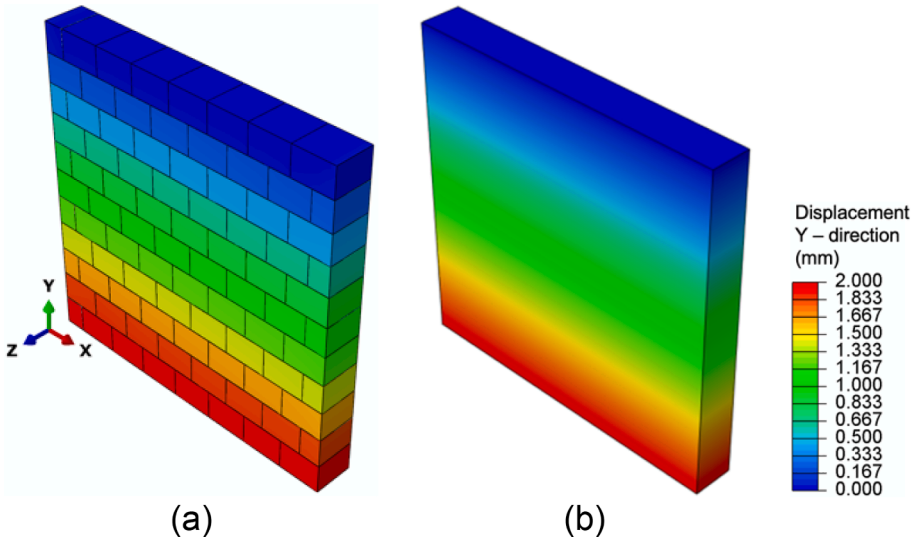

Fig. 12. Test series S01 - uniaxial loading and unloading - normal to bed joints: Displacement distribution along the Y direction (mm) at the peak force: a) micro-model; b) macro-model.

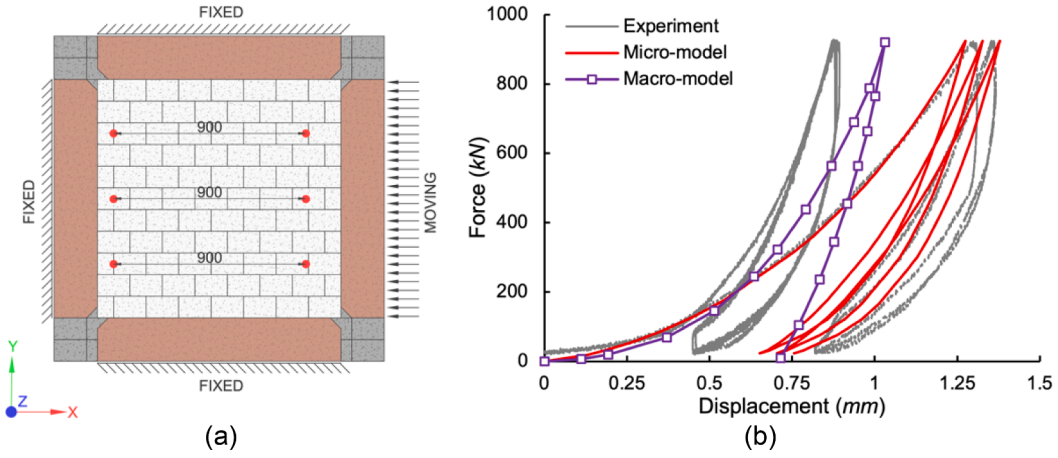

Fig. 13. Test series S02 - uniaxial loading and unloading - normal to head joints: a) boundary conditions; b) experimental and numerical force–displacement diagrams.

It can be observed from the results of the micro-model that almost all the displacement occurs due to the closing of dry joints, and bricks behave as a rigid unit for this low level of stress applied.

4.2. Test series S02 - uniaxial loading and unloading - normal to head joints

Regarding this test series, two refractory masonry walls were tested at room temperature [38]. The main difference between S02 and S01 is that the uniaxial compression loading (6 MPa) and unloading were applied to the direction normal to head joints. In contrast, the direction of the bed joints was constrained by the ceramic plungers. The boundary conditions of two fixed rigid plates, the moving rigid plate in the direction of the bed joints (Y direction in Fig. 13a) and the ground, are fully fixed.

Comparisons between the experimental and the numerical force–displacement diagrams of the walls subjected to uniaxial compression loading/unloading in the direction normal to head joints are given in Fig. 13b. The numerical models were able to predict the mechanical behaviour of the walls (for both the loading and unloading) with reasonable accuracy. When compared to S01, the value of the displacement at the maximum load level is lower. This can be attributed to the number of head joints in the wall being less than the number of bed joints (seven head joints and ten bed joints). This leads to higher stiffness (and, therefore, smaller deformation at the same load level) in the direction normal to head joints as compared to the direction normal to bed joints. After unloading, and as observed in S01, the walls did not return to the initial configuration, and there was permanent deformation.

Fig. 14a and b show the displacement fields obtained using both modelling approaches in the walls at maximum load level. In the micro-model, the bricks behave almost as rigid units for a low level of stress. However, similar range of displacments can be observed between the micro and macro modelling approach.

4.3. Test series S03 - biaxial loading and unloading

In this test series, two refractory masonry walls were tested at room temperature [38]. A 6 MPa biaxial compression load/unload was applied to the directions normal to bed and head joints. The boundary conditions of the ground and the two fixed rigid plates are fully fixed (Fig. 15a).

Fig. 15b presents a comparison between the experimental and numerical force–displacement diagrams in the directions normal to bed and head joints during loading and unloading. The present numerical models can reproduce with reasonable accuracy the orthotropic displacement stiffening mechanical behaviour of the wall. The reaction force increases with an increase in displacement due to the gradual closure of the joints and an increase in material stiffness with the gradual closure of joints. The maximum displacement in the direction normal to head joints is smaller than that in the direction normal to bed joints because the number of head joints is less than the number of bed joints. Similar to S01 and S02, there were permanent deformations in the directions normal to bed and head joints after load removal.

Fig. 16 makes the same observation as in Series S01 and S02, where bricks are almost rigid units for a low-stress level. However, lower values of displacement can be observed in both directions as compared to the results obtained from the uniaxial tests. This global displacement reduction can be explained by the high friction forces (caused by the biaxial loading conditions) and the reduced level of stresses experienced by the masonry in these biaxial loading conditions.

Fig. 17 shows the distribution of the principal compressive stress at the first peak load. From the figure, it is possible to observe the low level of stress in the masonry units except for the areas near the support plates. This reduction in the stresses is due to the presence of biaxial loads. In this case, the force is transferred through the combination of shear and normal stresses in the masonry. The shear stresses are experienced primarily near the support and loading plates. Therefore, the masonry units undergo a lower level of stress than the applied stress at the peak level.

Fig. 18 presents the distribution of principal compressive stress distribution in the refractory brick units at the centre of the wall during the peak force level in the biaxial test. It can be observed that the stress in the centre of the brick unit is around 5.2 MPa. Stresses increase to 6 MPa near the bed joints (Y direction) and reduce to 3 MPa near the head joints (X direction). This difference is due to the behaviour of the dry joints. The bed joints are continuous in the masonry, while the head joints are not. Therefore, bed joints experience lower restrictive shear forces through the nearby head joints, while the behaviour of head joints is highly influenced by the shear forces in the bed joints due to friction between the bricks. This behaviour also reduces displacement in the X direction (normal to the head joints) compared to the displacement in the Y direction (normal to the bed joints).

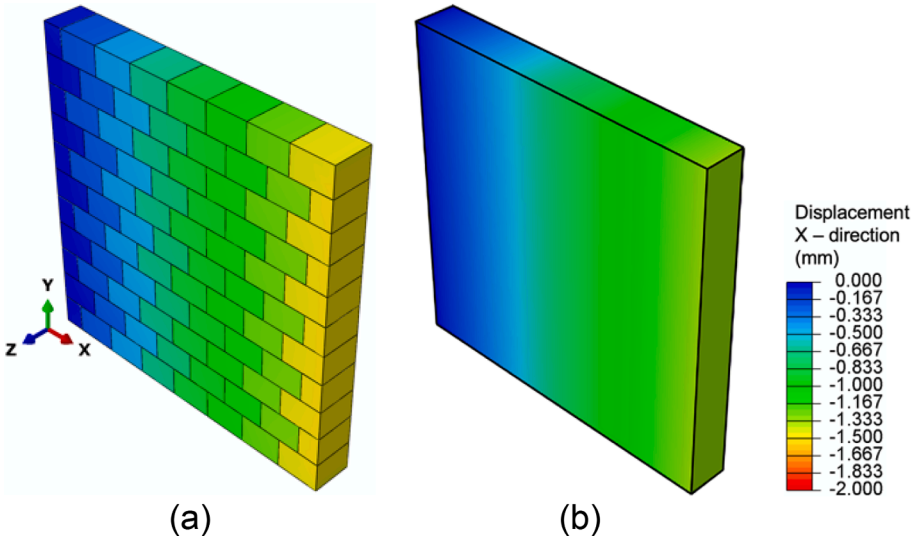

Fig. 14. Test series S02 - uniaxial loading and unloading - normal to head joints: Displacement distribution along the X direction (mm) at the peak force: a) micro-model; b) macro-model.

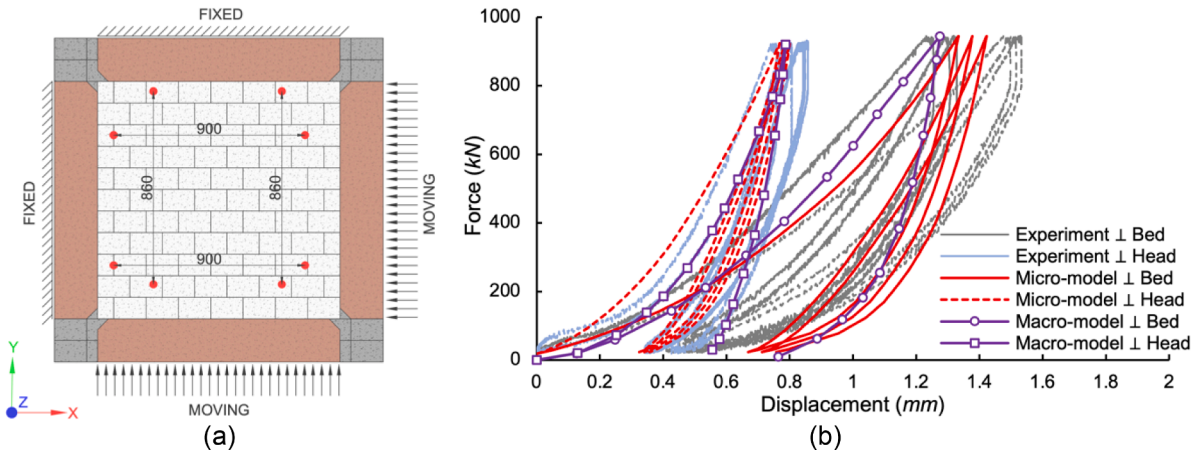

Fig. 15. Test series S03 - biaxial loading and unloading: a) boundary conditions; b) experimental and numerical force–displacement diagrams.

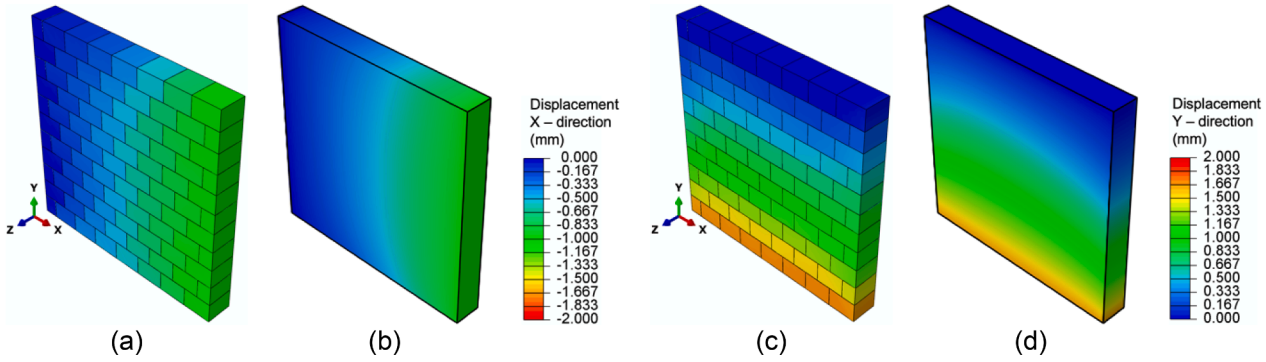

Fig. 16. Test series S03 - biaxial loading and unloading: Displacement along the X direction (mm) at the peak force level: a) micro-model; b) macro-model. Displacement along the Y direction (mm) at the peak force level: c) micro-model; d) macro-model.

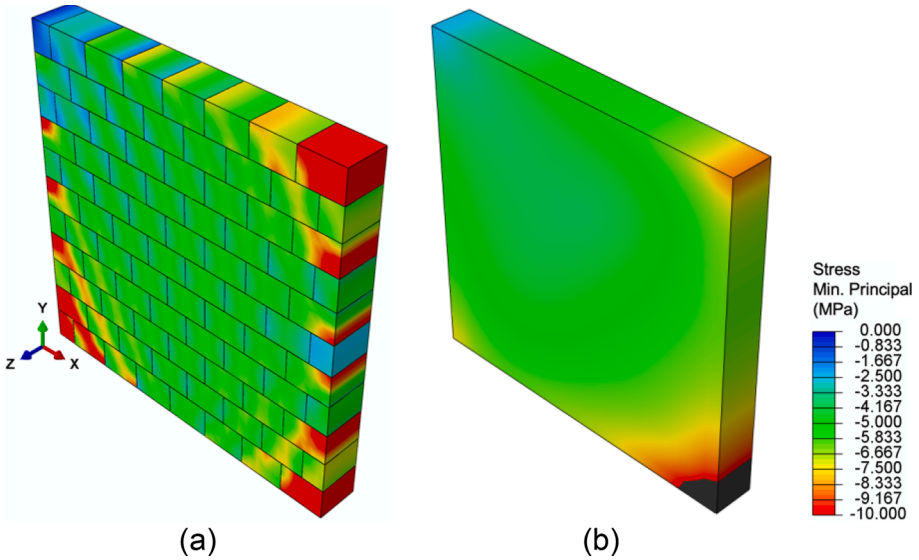

Fig. 17. Biaxial loading and unloading - minimum principal stress distribution (MPa) at the peak force level: a) micro-model; b) macro-model.

5. Numerical analyses at high temperature

Several refractory masonry walls were tested in these series under various thermomechanical loading conditions at high temperatures (as indicated in Table 1 and [38]). These experiments aimed at evaluating the orthotropic nonlinear elastic-viscoplastic behaviour of refractory masonry at temperatures of around 1500 °C (similar to in-service temperatures). The micro and macro FE modelling approaches were used to predict and then give more insights into the complex thermomechanical behaviour of the walls. The solution domains used for both these approaches are similar to those used in the previous section (Fig. 10). The temperature-dependent values of Youngs' modulus are used, as shown

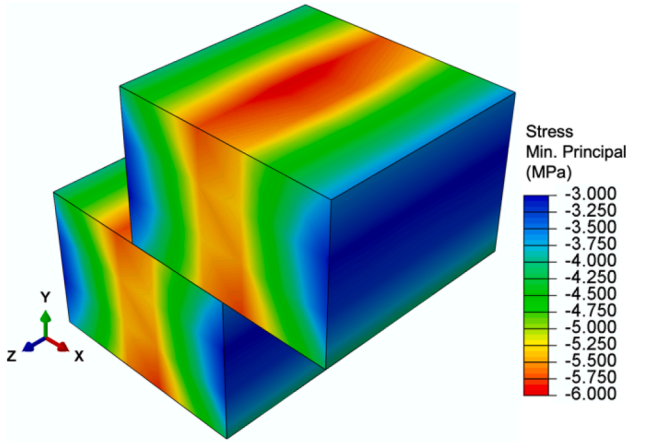

Fig. 18. Minimum principal stress distribution (MPa) in the masonry units at the centre of the wall at the peak force level.

in Fig. 2a. For viscoplasticity, creep parameters mentioned in Table 3 were used. Again, the frictional interactions were considered with a friction coefficient of 0.5.

The FE analysis of the walls comprises two steps: first, transient heat transfer analysis was carried out to compute the temperature distributions and variations with time, and second, transient thermo-mechanical analysis to calculate the resulting thermomechanical stress and strain fields. In the transient heat transfer analysis, the average measured temperature variations of the cold face (CF) and hot face (HF) of the walls were applied as thermal boundary conditions [38]. Therefore, the computed temperatures of the HF and the CF are the same as the applied temperature boundary conditions. The goal was to obtain the temperature fields through the thickness of the wall during heating, load application, holding and unloading. These, in turn, are employed as thermal loads in thermomechanical analysis. Comparisons between the experimental and numerical HF and CF temperature variations with time are given in Fig. 19a. The envelop for the CF represent the temperatures measured by the thermocouples.

In the thermomechanical analysis, during heating, load application and load holding and unloading steps, the boundary conditions of two fixed rigid plates and the ground (top insulation layer in the test field) are set to fully fixed. During heating, the two moving rigid plates were free to move (Fig. 19b). Then, during load application, load holding and unloading steps, the measured experimental reaction forces were applied as concentrated loads to the rigid moving plates.

The obtained temperature fields of the wall and the deformed shape (for both micro and macro modelling approaches), by the end of the heating step, due to thermal expansion effects, are given in Fig. 20. Higher values of a thermal expansion near the HF compared to the CF can be observed from the figure due to the higher temperature of the HF. As a result, the sides of the wall (in contact with the moving and fixed plungers) were not perfectly parallel to the plunger linings (wedged shape, in the depth of the wall) before the load application. The effect of thermal expansion is more significant in the macro-model (Fig. 20b) compared to the micro-model (Fig. 20a). This difference is due to the presence of the dry joint in the masonry, where the closing of the dry joints absorbs some extent of the expansion which differs considering the modelling approach. However, a similar wedged shape can be observed in both models, resulting in higher loads concentration at the HF during the initial loading period. The thermomechanical results obtained from both models for various loading conditions are presented in the following sections.

5.1. *Test series S04 - uniaxial creep behaviour - normal to bed joints*

In this test series, two refractory masonry walls were tested [38]. A uniaxial compression load/unload of 4 MPa was applied in the direction normal to bed joints after the heating stage and reaching thermal equilibrium. As explained in the previous section, the two rigid plates and the ground were fixed during heating and mechanical testing. During the load application, holding and unloading steps, the experimentally measured forces were applied to the two moving rigid plates (Fig. 21a).

Fig. 21b presents comparisons between the experimental and numerical displacement - time diagrams during loading, holding and unloading steps. Good agreement between the numerical and the experimental results can be observed. During loading, a rapid increase in the displacement can be observed due to the gradual closure of joints with increasing the applied load. This increase in the displacement is higher as compared to the room temperature uniaxial compression tests in the direction normal to bed joints (S01) due to the high bulk temperature of the specimen and, therefore, lower values of Young's modulus and creep as compared to series S01. During the holding step, an increase in the displacement of around 11 mm can be observed. This increase was mainly caused by viscoplasticity. Finally, the displacement decreased slightly during the unloading step. After load removal, the recovered displacement was minimal as compared to the displacement

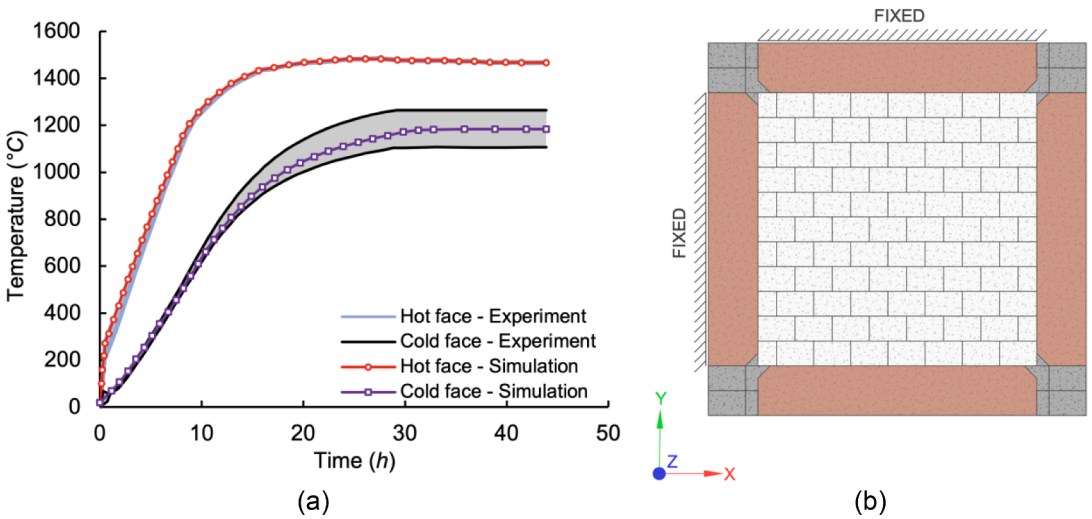

Fig. 19. Thermomechanical analysis: a) time variations of the cold and hot face temperatures during heating and mechanical testing, experimental and numerical results; b) boundary conditions for thermomechanical analysis during heating.

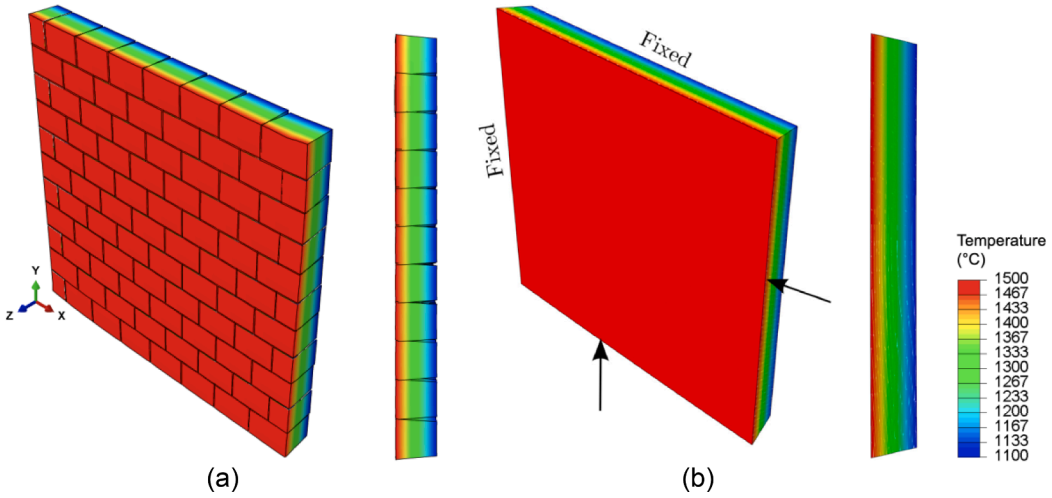

Fig. 20. Temperature distributions of the masonry wall by the end of the heating step showing the deformation of the wall due to thermal expansion: a) micro-model; b) macro-model.

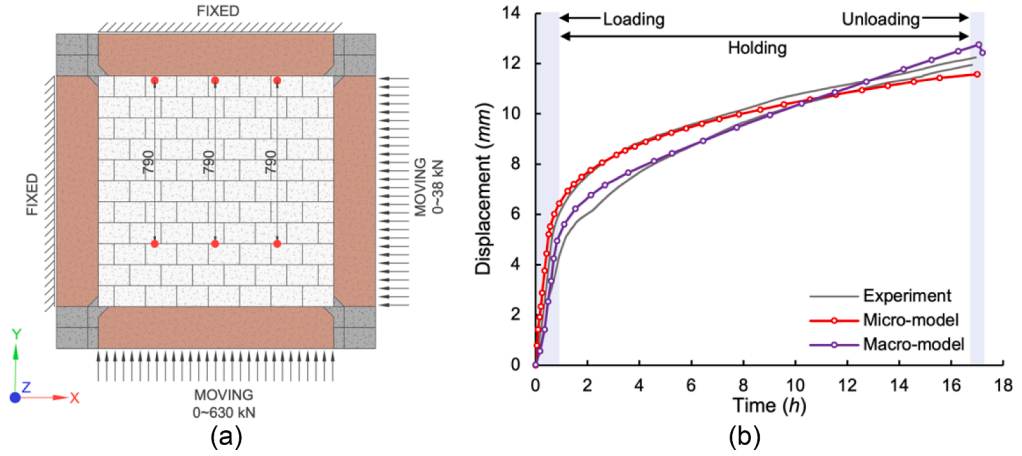

Fig. 21. Test series S04 - uniaxial creep behaviour - normal to bed joints: a) boundary conditions; b) experimental and numerical time variations of the displacements during loading, holding and unloading stages.

due to the applied load. This can be attributed to the permanent deformation resulting from the viscoplastic behaviour of the structure and joint closure. The slight difference between the experimental and numerical values is mainly due to the creep parameters. It should be noted that, in the micro-modelling approach, only the primary creep parameters are used, while in the macro-model secondary creep parameters are used.

Fig. 22a and b show displacement fields in the direction of normal to bed joints obtained using the micro and macro modelling approaches. From Fig. 22a (micro modelling), it can be observed that at high temperatures, the bricks do not behave as rigid units as it was observed in the room temperature tests. This is due to material property degradation and creep effects at higher temperatures. The distributions of minimum principal stresses by the end of the load holding step are shown in Fig. 22c and d. It can be seen from the figures that the stresses observed on the HF are lower as compared to those in the CF. This can be

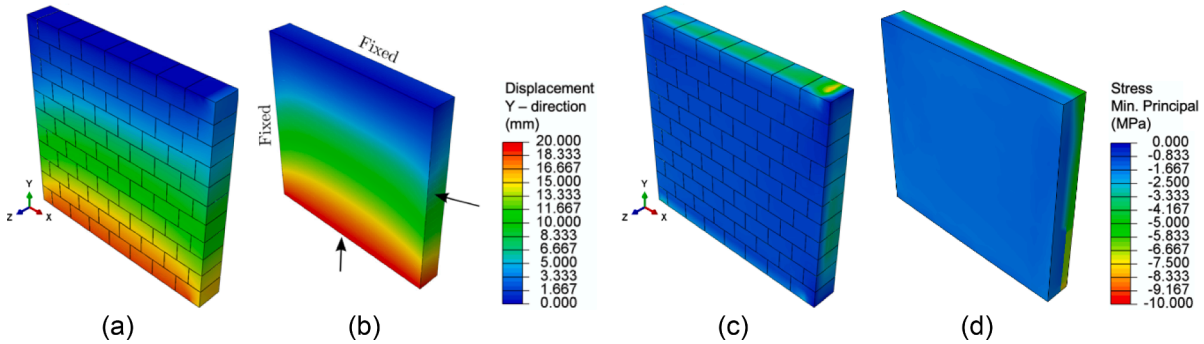

Fig. 22. Test series S04 - uniaxial creep behaviour - normal to bed joints: Displacement distribution along the Y direction (mm) at 16th hour: a) micro-model; b) macro-model. Minimum principal stress distribution (MPa) at 16th hour: c) micro-model; d) macro-model.

attributed to the lower temperature of the CF and, therefore, lower creep rates as compared to the HF; higher viscoplastic deformation rates were observed in the HF as compared to the CF. This led to a decay in the stresses in the HF due to stress relaxation and an increase in the stresses in the CF during the holding step.

5.2. Test series S05 - uniaxial creep behaviour - normal to head joints

The significant difference between S05 and S04 is that the uniaxial compression load was applied in the direction normal to head joints. In contrast, the other direction was constrained by the ceramic plungers (direction normal to bed joints). A uniaxial compression load/unload of 4 MPa was applied in the direction normal to head joints after the heating. During the load application, holding and unloading, the experimentally measured forces were applied as concentrated loads to the other two moving rigid plates (Fig. 23a).

Comparisons between the experimental and numerical displacement - time diagrams during loading, holding and unloading steps are given in Fig. 23b. Good agreements between the numerical and the experimental results can be observed. During loading, a rapid increase in the displacement can be seen due to the gradual closure of joints with increasing the applied load. The increase in the displacement is higher compared to the test performed at ambient temperature (S02) because of the lower values of Young's modulus at high temperature and the contribution of viscoplasticity to the total displacement during loading. Then, during the holding step, an increase in the displacement can be observed due to creep. Finally, the displacement decreased slightly due to unloading. After load removal, the recovered displacement is very small as compared to the displacement measured during the load application step. This is caused by the viscoplastic deformation and closure of joints. It should be noted that in the case of test series S04 and test series S05, the increase in the displacement during the holding time is almost equal. This can be attributed to that, in both cases, after load application, the joints in the loading direction (bed joints in the case of S04 and head joints in the case of S05) are almost closed, and when joints are closed, the behaviour of the wall is similar to that of the bricks (i.e. similar behaviour in both cases) [19,20].

Fig. 24 shows the displacement fields by the end of the load holding stage in the direction normal to head joints obtained using the micro and macro modelling approaches. Similar distributions to those of test series S04 can be observed. For the displacement fields obtained using the micro modelling approach, the bricks do not behave as rigid units due to reduced material stiffness and creep at high temperatures. The minimum principal stress distributions obtained using both modelling techniques are given in Fig. 24c and d. They are similar to those observed in test series S04 due to the similar applied load level. Lower values of stresses at the HF are observed as compared to those in the CF due to the higher HF temperature and, therefore, lower values of Young's modulus and stress relaxation effects caused by the wedge shape of the wall.

5.3. Test series S06 - biaxial creep behaviour

To evaluate the creep behaviour under biaxial loading conditions, two refractory walls were tested at high temperatures [38]. The FE models and boundary conditions are the same as in the previous sections. After the load application step, the applied forces were held constant for 16 h. During the load application, holding and unloading, experimentally measured forces were applied to the two moving rigid plates (Fig. 25a).

Comparisons between the experimental and numerical displacement – time diagrams in the directions normal to bed and head joints during loading, holding and unloading steps are shown in Fig. 25b. Good agreements between the experimental and numerical results can be observed. The maximum displacement in the direction normal to bed joints is higher as compared to that in the direction normal to head joints due to the difference between the number of bed and head joints in the wall. However, the observed displacements are lower compared to the uniaxial creep tests performed at high temperatures. This reduction is due to biaxial force application on the refractory masonry wall, which generates lower stresses in the materials and higher friction forces with the loading beams. During the holding time, the increase in the displacements in both directions was almost the same, indicating full closure of bed and head joints during the loading step and, therefore, isotropic in-plane viscoplastic behaviour.

The displacement fields, by the end of the load holding step, in the direction normal to bed and head joints obtained using the micro and macro modelling approaches are shown in Fig. 26. The minimum principal stress fields, by the end of the load holding step, in the direction normal to bed and head joints obtained using the micro and macro modelling approaches are shown in Fig. 27. Compared to S04 and S05, similar observations of σ_{bed} CF, HF and σ_{head} CF, HF can be observed. However, the stresses observed in this test series are lower as compared to the stresses observed in the previous uniaxial creep tests normal to bed and head joints.

5.4. Test series S07 - biaxial relaxation behaviour

The goal of this test series was to investigate the relaxation behaviour of the walls at high temperatures. Therefore, constant strain loading conditions were employed. The modelling technique is similar to previous sections for both modelling approaches. During heating, the mechanical boundary conditions of the plungers and the ground are

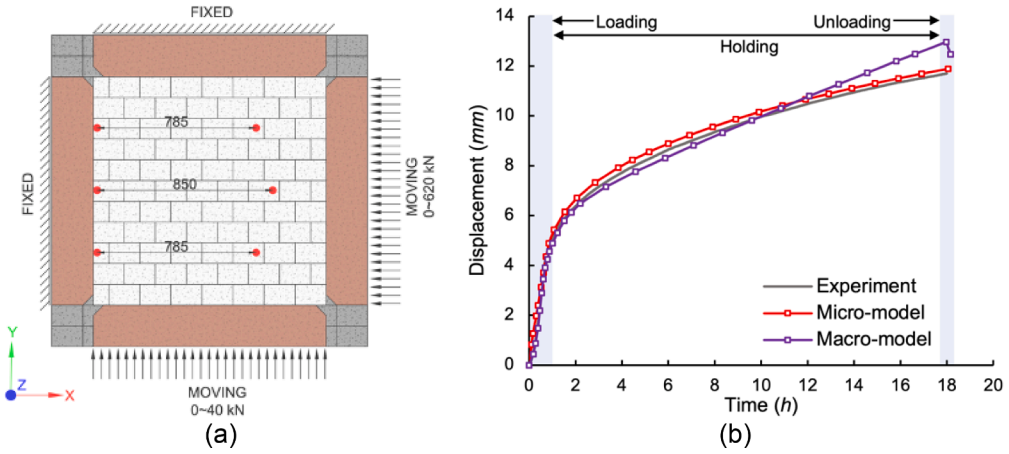

Fig. 23. Test series S05 - uniaxial creep behaviour - normal to head joints: a) boundary conditions; b) experimental and numerical time variations of the displacements during loading, holding and unloading stages.

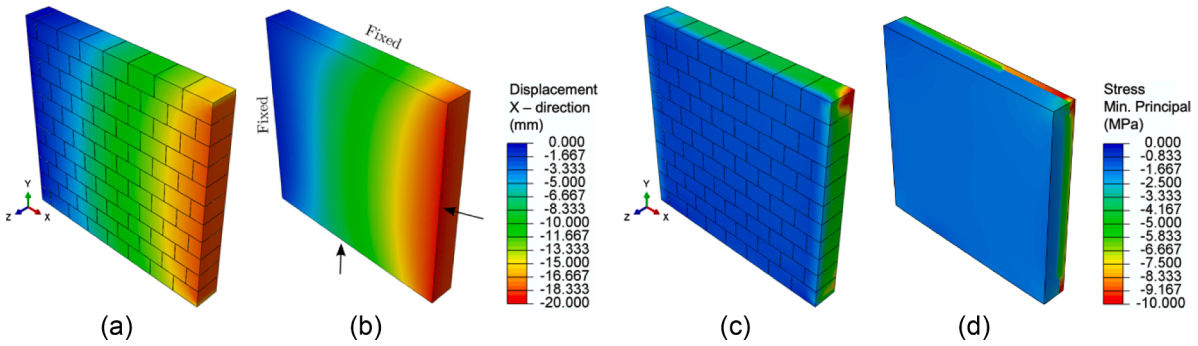

Fig. 24. Test series S05 - uniaxial creep behaviour - normal to bed joints: Displacement distribution along the X direction (mm) at 16th hour: a) micro-model; b) macro-model. Minimum principal stress distribution (MPa) at 16th hour: c) micro-model; d) macro-model.

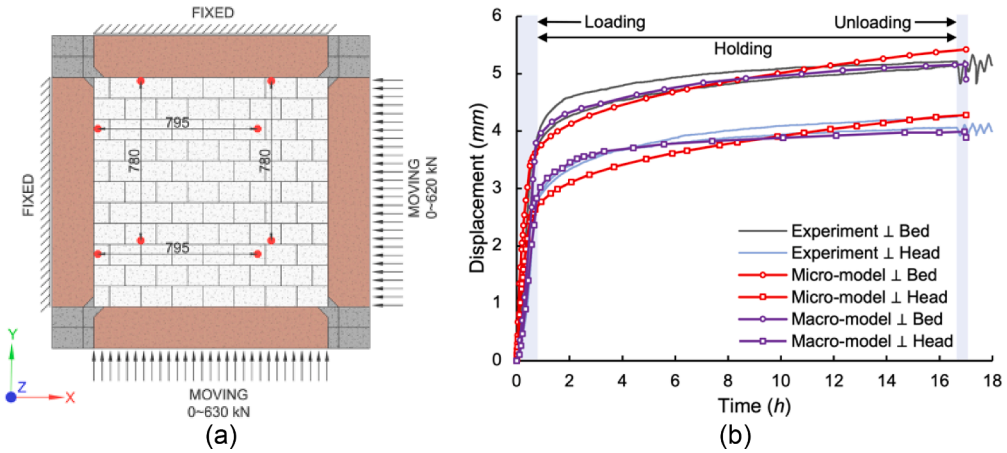

Fig. 25. Test series S06 - Biaxial creep behaviour: a) boundary conditions; b) experimental and numerical time variations of the displacements during loading, holding and unloading stages.

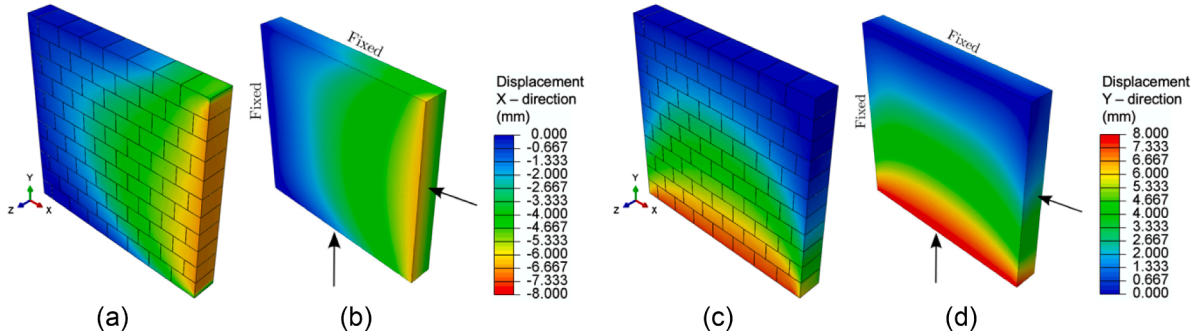

Fig. 26. Test series S06 - biaxial loading and unloading: Displacement along the X direction (mm): a) micro-model; b) macro-model. Displacement along the Y direction (mm): c) micro-model; d) macro-model.

identical to Fig. 19b. During loading, the boundary conditions are almost the same as in Fig. 25a with only one difference; displacement boundary conditions were applied to the moving plungers instead of concentrated forces and kept constant during the holding time.

Comparisons between the experimental and numerical time variations of the resulting reaction forces, in the directions normal to bed and head joints, during two loading/unloading cycles are reported in Fig. 28. Good agreements between the experimental and numerical results can be observed. During loading (1st cycle), the resulting reaction forces increased gradually to reach 600 kN. Then, when the position of the plungers is locked, a decay in the resulting reaction forces was observed due to stress relaxation caused by the viscoplastic behaviour of the structure at high temperatures. Then, the forces decreased to zero during the unloading stage. Similar behaviour was noticed for the second loading cycle.

6. Conclusion

Refractory masonry with dry joints exhibits complex behaviour. Numerical simulations are the most cost-effective way to understand such behaviour, including joint closing and opening, creep and relaxation at high temperatures. However, calibration and validation of such models are required to analyse the behaviour accurately with the experimental results. Moreover, large-scale experiments are scarce for refractory masonry. Therefore, based on the large-scale experimental campaign carried out within the framework of the ATHOR project [38],

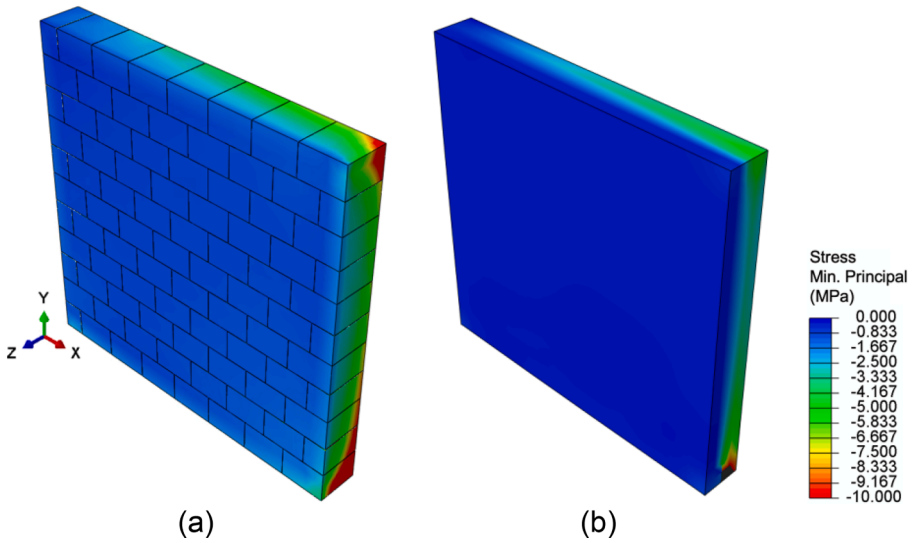

Fig. 27. Biaxial loading and unloading - minimum principal stress distribution (MPa) at the 16th hour of holding: a) micro-model; b) macro-model.

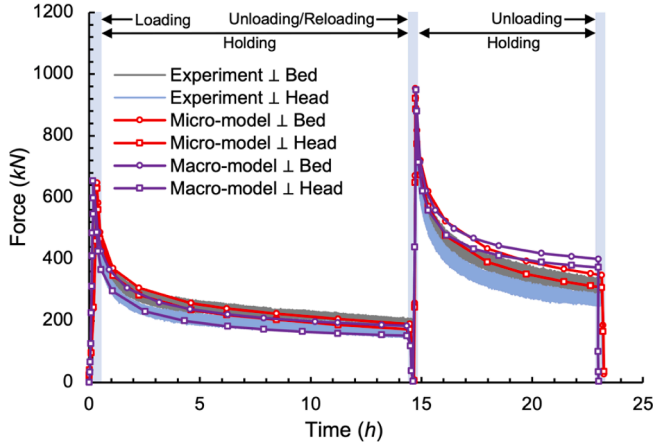

Fig. 28. Experimental and numerical time variations of reaction forces during loading, holding and unloading stages of two testing cycles.

numerical models with different modelling approaches were developed and validated.

This paper presents a comparison between two modelling approaches, the homogenisation approach (macro-modelling) and the micro-modelling approach. The macro-modelling approach replaces refractory brick units and dry joints with an equivalent homogenised material. The micro-modelling approach models both the units and joints between units. The results obtained from both approaches show a good agreement with the experimental results.

The results presented here show that both modelling approaches provide a reliable prediction of masonry response at the ambient and high temperatures, validated by the experimental results. Moreover, the response obtained by these approaches are in good agreement with each other. For the simulations, both models employ the same parameter values for the thermomechanical properties of the materials and similar boundary conditions. The primary difference between the models was the joint closure relation. Despite this difference, the numerical responses of these models were well within the bounds of experimental results.

In mortarless masonry, the distribution of dry joints is influenced by the surface asperities, manufacturing tolerances and construction technique. Thus, the dry joint thickness is non uniform. The joint closing behaviour of the dry joint is essential to characterise the orthotropic global behaviour of the mortarless masonry at ambient temperature. The dry joint is also crucial during the thermal loading as it provides a break in the continuum and reduces stresses induced by thermal expansion by allowing bricks to expand freely till the limit of joint thickness. As in the case of industrial structures, the refractory masonry is subjected to thermal gradient within its thickness. Therefore, the hot face will expand more when compared to the cold face. Consequently, during loading, the hot face will undergo loading first and depending on the viscoplastic behaviour, the force will be transferred from the hot face to the cold face. The comparison between the models in terms of displacement and stress distributions shows that the formulation used for modelling joint behaviour as well as to compensate of thermal expansion in the macro model is accurate and can define global behaviour of mortarless masonry at higher temperature.

Therefore, both approaches can be used for the thermomechanical analyses of refractory structures. Depending on the outcome requirement, a particular approach can be selected. A homogenized model uses a more straightforward geometry modelling compared to micro-modelling, where all the individual units and interfaces must be modelled separately which significantly increases the number of elements in the model. Due to the presence of interface elements in the micro model, the load or temperature increment has to be small to avoid discontinuity problems during analysis to achieve accurate results, thus increasing the computational cost. In contrast, the macro model described in this work can give accurate results while using larger increments during analysis with less computational cost. This can be useful while modelling larger industrial structures where the primary focus is on global behaviour.

In general, compared to micro-models, homogenized models require fewer parameters to define the materials during the analysis. Additional parameters need to be defined in micro-models, depending on the constitutive models used. However, the homogenised approach presented in this document requires the formulation of various equations to identify the stiffness parameters of the homogenised elements and a user-supplied subroutine. Therefore, both modelling approaches require similar inputs for material and geometric parameters with a difference that macro model utilises some of these data for the formulation of stiffness parameters.

As presented in this document, the macro-modelling approach provides useful global outputs. In contrast, micro-models can provide, besides global outputs, localised output as well (for example, stress and strain concentration near the joints, localised damage, and deformation). Thus, micro-model can be used in an application where the

detailed description of material behaviour is required, for instance in preliminary analysis to select different materials of the refractory linings in a steel ladle. It should be highlighted that these modelling approaches can be used in combination. A global response obtained from the homogenised approach can be used to supply a localised boundary condition for a small part of a large structure to evaluate the localised behaviour of the refractory masonry.

CRediT authorship contribution statement

Pratik N. Gajjar: Conceptualization, Investigation, Validation, Formal analysis, Writing – original draft. **Mahmoud Ali:** Conceptualization, Investigation, Validation, Formal analysis, Writing – original draft. **Thomas Sayet:** Conceptualization, Validation, Writing – review & editing, Supervision, Project administration, Funding acquisition. **Alain Gasser:** Conceptualization, Validation, Writing – review & editing, Supervision, Project administration, Funding acquisition. **Eric Blond:** Conceptualization, Validation, Writing – review & editing, Supervision, Project administration, Funding acquisition. **João M. Pereira:** Conceptualization, Validation, Writing – review & editing, Supervision, Project administration, Funding acquisition. **Paulo B. Lourenço:** Validation, Writing – review & editing, Supervision, Project administration, Funding acquisition.

Declaration of Competing Interest

The authors declare that they have no known competing financial interests or personal relationships that could have appeared to influence the work reported in this paper.

Data availability

Data will be made available on request.

Acknowledgement

This work was supported by the funding scheme of the European Commission, Marie Skłodowska-Curie Actions Innovative Training Networks in the frame of the project ATHOR - Advanced THermo-mechanical multiscale mOdelling Refractory linings 764987 Grant. The first, sixth and seventh author also acknowledge the financial support by FCT / MCTES through national funds (PIDDAC) under the R&D Unit Institute for Sustainability and Innovation in Structural Engineering (ISISE), under reference UIDB / 04029/2020, and under the Associate Laboratory Advanced Production and Intelligent Systems ARISE under reference LA/P/0112/2020. This work is financed by national funds through FCT - Foundation for Science and Technology, under grant agreement 2021.05961.BD attributed to the first author.

References

[1] Blond E, Nguyen AK, de Bilbao E, Sayet T, Batakis A. Thermo-chemo-mechanical modeling of refractory behavior in service: Key points and new developments. Int J Appl Ceram Technol 2020;17:1693–700. https://doi.org/10.1111/IJAC.13499.
[2] Chen J, Chen L, Wei Y, Li N, Zhang S. Corrosion and penetration behaviors of slag/steel on the corroded interfaces of Al2O3-C refractories: Role of Ti3AlC2. Corros Sci 2018;143:166–76. https://doi.org/10.1016/J.CORSCI.2018.08.022.
[3] Andreev K, Luchini B, Rodrigues MJ, Alves JL. Role of fatigue in damage development of refractories under thermal shock loads of different intensity. Ceram Int 2020;46:20707–16. https://doi.org/10.1016/J.CERAMINT.2020.04.235.
[4] Schacht CA. Refractory lining: Thermomechanical design and applications. Mech Eng 1995.
[5] Blond E, Schmitt N, Hild F, Blumenfeld P, Poirier J. Effect of Slag Impregnation on Thermal Degradations in Refractories. J Am Ceram Soc 2007;90:154–62. https://doi.org/10.1111/J.1551-2916.2006.01348.X.
[6] Samadi S, Jin S, Gruber D, Harmuth H, Schachner S. Statistical study of compressive creep parameters of an alumina spinel refractory. Ceram Int 2020;46:14662–8. https://doi.org/10.1016/j.ceramint.2020.02.267.
[7] Harmuth H, Rieder K, Krobath M, Tschegg E. Investigation of the nonlinear fracture behaviour of ordinary ceramic refractory materials. Mat Sci and Engineering 1996;A214:53–61. https://doi.org/10.1016/0921-5093(96)10221-5.
[8] Tschegg E k., Fendt KT, Manhart C, Harmuth H. Uniaxial and biaxial fracture behaviour of refractory materials. Eng Fract Mech 2009;76:2249–59. 10.1016/j.engfracmech.2009.07.011.
[9] Jin S, Harmuth H, Gruber D. Compressive creep testing of refractories at elevated loads—Device, material law and evaluation techniques. J Eur Ceram Soc 2014;34:4037–42. https://doi.org/10.1016/J.JEURCERAMSOC.2014.05.034.
[10] Teixeira L, Samadi S, Gillibert J, Jin S, Sayet T, Gruber D, et al. Experimental Investigation of the Tension and Compression Creep Behavior of Alumina-Spinel Refractories at High Temperatures. Ceramics 2020:3. https://doi.org/10.3390/ceramics3030033.
[11] Brosnan DA. Alumina-Silica brick. In: Schacht CA, editor. Refractories Handbook. 1st ed. CRC Press; 2004. p. 79–108. https://doi.org/10.1201/9780203026328.
[12] Revie RW. Uhlig's Corrosion Handbook. John Wiley and Sons; 2011. https://doi.org/10.1002/9780470872864.
[13] Gruber D, Harmuth H. Thermomechanical behavior of steel ladle linings and the influence of insulations. Steel Res Int 2014;85:512–8.
[14] Andreev K, Sinnema S, Rekik A, Allaoui S, Blond E, Gasser A. Compressive behaviour of dry joints in refractory ceramic masonry. Constr Build Mater 2012;34:402–8. https://doi.org/10.1016/J.CONBUILDMAT.2012.02.024.
[15] Allaoui S, Rekik A, Gasser A, Blond E, Andreev K. Digital Image Correlation measurements of mortarless joint closure in refractory masonries. Constr Build Mater 2018;162:334–44. https://doi.org/10.1016/J.CONBUILDMAT.2017.12.055.
[16] Oliveira RLG, Rodrigues JPC, Pereira JM, Lourenço PB, Ulrich MH. Normal and tangential behaviour of dry joints in refractory masonry. Eng Struct 2021;243:112600. https://doi.org/10.1016/j.engstruct.2021.112600.
[17] Gasser A, Terny-Rebeyrotte K, Boisse P. Modelling of joint effects on refractory lining behaviour. Proc Instit Mech Eng Part L: J Mater: Des Appl 2004;218:19–28. https://doi.org/10.1243/146442004322849881.
[18] Nguyen TMHH, Blond E, Gasser A, Prietl T. Mechanical homogenisation of masonry wall without mortar. Eur J Mech-A/Solids 2009;28:535–44. https://doi.org/10.1016/j.euromechsol.2008.12.003.
[19] Ali M, Sayet T, Gasser A, Blond E. Transient Thermo-Mechanical Analysis of Steel Ladle Refractory Linings Using Mechanical Homogenization Approach. Ceramics 2020 2020;3:171–89. https://doi.org/10.3390/ceramics3020016.
[20] Ali M, Sayet T, Gasser A, Blond E. Computational Homogenization of Elastic-Viscoplastic Refractory Masonry with Dry Joints. Int J Mech Sci 2021;196:106275. https://doi.org/10.1016/j.ijmecsci.2021.106275.
[21] Prietl T. Determination of material-specific parameters of refractory materials and linings under uniaxial and biaxial load conditions for the non-ferrous metal industry - in German. Austria: Montanuniversität Leoben; 2006. PhD thesis.
[22] Oliveira RLG, Rodrigues JPC, Pereira JM, Lourenço PB, Marschall HU. Thermomechanical behaviour of refractory dry-stacked masonry walls under uniaxial compression. Eng Struct 2021:240. https://doi.org/10.1016/j.engstruct.2021.112361.
[23] Oliveira R, Rodrigues JP, Pereira J, Lourenço PB, Lopes R. Experimental and numerical analysis on the structural fire behaviour of three-cell hollowed concrete masonry walls. Eng Struct 2021;228:111439. https://doi.org/10.1016/j.engstruct.2020.111439.
[24] Portioli F, Cascini L. Large displacement analysis of dry-jointed masonry structures subjected to settlements using rigid block modelling. Eng Struct 2017;148:485–96. https://doi.org/10.1016/J.ENGSTRUCT.2017.06.073.
[25] Casapulla C, Argiento LU. In-plane frictional resistances in dry block masonry walls and rocking-sliding failure modes revisited and experimentally validated. Compos B Eng 2018;132:197–213. https://doi.org/10.1016/J.COMPOSITESB.2017.09.013.
[26] Foti D, Vacca V, Facchini I. DEM modeling and experimental analysis of the static behavior of a dry-joints masonry cross vaults. Constr Build Mater 2018;170:111–20. https://doi.org/10.1016/J.CONBUILDMAT.2018.02.202.
[27] Grillanda N, Chiozzi A, Milani G, Tralli A. Tilting plane tests for the ultimate shear capacity evaluation of perforated dry joint masonry panels. Part II: Numerical analyses Eng Struct 2021;228:111460. https://doi.org/10.1016/J.ENGSTRUCT.2020.111460.
[28] Pulatsu B, Gonen S, Erdogmus E, Lourenço PB, Lemos JV, Prakash R. In-plane structural performance of dry-joint stone masonry Walls: A spatial and non-spatial stochastic discontinuum analysis. Eng Struct 2021;242:112620. https://doi.org/10.1016/J.ENGSTRUCT.2021.112620.
[29] Mendes N, Zanotti S, Lemos JV. Seismic Performance of Historical Buildings Based on Discrete Element Method: An Adobe Church 2018;24:1270–89. https://doi.org/10.1080/1363246920181463879.
[30] Gobbin F, de Felice G, Lemos JV. A Discrete Element Model for Masonry Vaults Strengthened with Externally Bonded Reinforcement 2020;15:1959–72. https://doi.org/10.1080/1558305820201743792.
[31] Lourenço PB, Gaetani A. Finite Element Analysis for Building Assessment advanced use and practical recommendations. ROUTLEDGE; 2022.
[32] Salachoris GP, Standoli G, Betti M, Milani G, Clementi F. Evolutionary numerical model for cultural heritage structures via genetic algorithms: a case study in central Italy. Bull Earthq Eng 2023:1–35. https://doi.org/10.1007/S10518-023-01615-Z/FIGURES/17.
[33] Lourenço PB, Silva L. Computational applications in masonry structures: from the meso-scale to the super-large/super-complex. Int J Multiscale Comput Eng 2020:18. https://doi.org/10.1615/IntJMultCompEng.2020030889.

[34] Andreev K, Harmuth H. FEM simulation of the thermo-mechanical behaviour and failure of refractories - A case study. J Mater Process Technol 2003;143–144:72–7. https://doi.org/10.1016/S0924-0136(03)00322-4.
[35] Gajjar PN, Pereira JM, Lourenço PB. Thermo-Mechanical Behavior of Refractory Masonry Linings: An Overview on Numerical Simulation. In: Dillon PB, Fonseca FS, editors. Proc. of Thirteenth North American Masonry Conference. Salt Lake City, Utah: The Masonry Society; 2019. p. 311–23.
[36] Prakash PR, Azenha M, Pereira JM, Lourenço PB. Finite element based micro modelling of masonry walls subjected to fire exposure: Framework validation and structural implications. Eng Struct 2020;213:110545. https://doi.org/10.1016/j.engstruct.2020.110545.
[37] Ali M, Sayet T, Gasser A, Blond E. A Multiscale Model for Numerical Modelling of Homogenized Elastic-Viscoplastic Behavior of Mortarless Refractory Masonry Structures. 14th World Congress in Computational Mechanics (WCCM), ECCOMAS Congress 2020, Paris (Virtual), France: 2021.
[38] Ali M, Oliveira RLG, Pereira JM, Rodrigues JP, Lourenço PB, Ulrich Marschall H, et al. Experimental characterization of the nonlinear thermomechanical behaviour of refractory masonry with dry joints. Constr Build Mater 2023;364:129960. https://doi.org/10.1016/J.CONBUILDMAT.2022.129960.
[39] Ali M. Nonlinear thermomechanical modelling of refractory masonry Linings. France: University of Orléans; 2021. PhD thesis.
[40] Kaczmarek R. Mechanical characterization of refractory materials. France: University of Limoges; 2021. PhD thesis.
[41] Vitiello D. Thermo-physical properties of insulating refractory materials. France: University of Limoges; 2021. PhD thesis.
[42] Smith M. ABAQUS/Standard User's Manual, Version 2019. United States: Dassault Systèmes Simulia Corp; 2019.
[43] Russo S, Sciarretta F. Masonry exposed to high temperatures: mechanical behaviour and properties—an overview. Fire Saf J 2013;55:69–86.
[44] Lourenço PB. Experimental and numerical issues in the modelling of the mechanical behaviour of masonry. Structural Analysis of Historical Constructions II 1998.
[45] Lourenço PB. Computational strategies for masonry constructions. Delft, The Netherlands: Delft Univ. Press; 1996. PhD thesis.
[46] Šejnoha J, Šejnoha M, Zeman J, Sýkora J, Vorel J. Mesoscopic study on historic masonry. Struct Eng Mech 2008;30:99–117. https://doi.org/10.12989/SEM.2008.30.1.099.
[47] Macorini L, Izzuddin BA. A non-linear interface element for 3D mesoscale analysis of brick-masonry structures. Int J Numer Methods Eng 2011;85:1584–608. https://doi.org/10.1002/NME.3046.
[48] Giambanco G, Rizzo S, Spallino R. Numerical analysis of masonry structures via interface models. Comput Methods Appl Mech Eng 2001;190:6493–511. https://doi.org/10.1016/S0045-7825(01)00225-0.
[49] Chewe Ngapeya GG, Waldmann D, Scholzen F. Impact of the height imperfections of masonry blocks on the load bearing capacity of dry-stack masonry walls. Constr Build Mater 2018;165:898–913. https://doi.org/10.1016/J.CONBUILDMAT.2017.12.183.
[50] Lubliner J, Oliver J, Oller S, Oñate E. A plastic-damage model for concrete. Int J Solids Struct 1989;25:299–326. https://doi.org/10.1016/0020-7683(89)90050-4.
[51] Lee J, Fenves GL. Plastic-Damage Model for Cyclic Loading of Concrete Structures. J Eng Mech 1998;124:892–900. https://doi.org/10.1061/(ASCE)0733-9399(1998)124:8(892).
[52] Vecchio FJ, Collins MP. The modified compression field theory for reinforced concrete elements subjected to shear. ACI J 1986;83:219–31.
[53] Mazars J, Pijaudier-Cabot G. Continuum Damage TheoryApplication to Concrete. J Eng Mech 1989;115:345–65. https://doi.org/10.1061/(ASCE)0733-9399(1989)115:2(345).
[54] Salachoris GP, Magagnini E, Clementi F. Mechanical characterization of "Scaglia Rossa" stone masonry through experimental and numerical analyses. Constr Build Mater 2021;303:124572. https://doi.org/10.1016/J.CONBUILDMAT.2021.124572.
[55] Samadi S, Jin S, Harmuth H. Combined damaged elasticity and creep modeling of ceramics with wedge splitting tests. Ceram Int 2021;47:25846–53. https://doi.org/10.1016/J.CERAMINT.2021.05.315.
[56] Lourenço PB, Rots JG, Blaauwendraad J. Two approaches for the analysis of masonry structures: micro and macro-modeling. HERON 1995;40(4):1995.
[57] Coulomb C. Essai sur une application des règles de maximis et minimis quelques problèmes de statique, relatifs à l'architecture. Mémoires de Mathématiques et de Physique de l'Académie Royale des Sciences 1776;7.
[58] Hill R. The essential structure of constitutive laws for metal composites and polycrystals. J Mech Phys Solids 1967;15:79–95. https://doi.org/10.1016/0022-5096(67)90018-X.
[59] Lourenço PB, Barros JO, Oliveira JT. Shear testing of stack bonded masonry. Constr Build Mater 2004;18:125–32.
[60] Tsuda M, Takemura E, Asada T, Ohno N, Igari T. Homogenized elastic-viscoplastic behavior of plate-fin structures at high temperatures: Numerical analysis and macroscopic constitutive modeling. Int J Mech Sci 2010;52:648–56. https://doi.org/10.1016/j.ijmecsci.2009.06.007.
[61] Tsuda M, Ohno N. Duplex model for homogenized elastic-viscoplastic behavior of plate-fin structures at high temperatures. Int J Plast 2011;27:1560–76. https://doi.org/10.1016/j.ijplas.2010.10.011.
[62] Xia Z, Zhou C, Yong Q, Wang X. On selection of repeated unit cell model and application of unified periodic boundary conditions in micro-mechanical analysis of composites. Int J Solids Struct 2006;43:266–78. https://doi.org/10.1016/j.ijsolstr.2005.03.055.